

Quantum mechanical study of the attosecond nonlinear Fourier transform spectroscopy of carbon dioxide

Sergy Yu. Grebenshchikov*

Rüsterstr. 24, 60325 Frankfurt am Main, Germany

Sergio Carbajo

SLAC National Accelerator Laboratory and Stanford University,

2575 Sand Hill Rd, Menlo Park, CA 94025, USA

Attosecond nonlinear Fourier transform (NFT) pump probe spectroscopy is an experimental technique which allows investigation of the electronic excitation, ionization, and unimolecular dissociation processes. The NFT spectroscopy utilizes ultrafast multiphoton ionization in the extreme ultraviolet spectral range and detects the dissociation products of the unstable ionized species. In this paper, a quantum mechanical description of NFT spectra is suggested, which is based on the second order perturbation theory in molecule-light interaction and the high level ab initio calculations of CO_2 and CO_2^+ in the Franck-Condon zone. The calculations capture the characteristic features of the available experimental NFT spectra of CO_2 . Approximate analytic expressions are derived and used to assign the calculated spectra in terms of participating electronic states and harmonic photon frequencies. The developed approach provides a convenient framework within which the origin and the significance of near harmonic and non-harmonic NFT spectral lines can be analyzed. The framework is scalable and the spectra of di- and triatomic species as well as the dependences on the control parameters can be predicted semi-quantitatively.

I. INTRODUCTION

Chemical transformations, induced by the ultraviolet (UV), vacuum UV (VUV), and extreme UV (XUV) light in carbon dioxide CO_2 and carbon dioxide cation CO_2^+ , are of considerable importance for atmospheric, planetary, and interstellar chemistry. Spectral

* Email: sgreben@gwdg.de

signatures of the cation CO_2^+ were detected in the Martian atmosphere and the comet comae and tails.^{1,2} CO_2 is the second common trace gas in the Earth atmosphere. It is one of the main products of the fossil fuel burning³ and its photoabsorption is used in the UV diagnostics of high-temperature and high-pressure flames.⁴ Accurate knowledge of its low-temperature UV absorption properties would improve the existing photochemical models of the atmospheres of Mars, which is to a 95% CO_2 -based,⁵ and of Titan,⁶ in which CO_2 is a minor constituent.

Structure, properties, and photodynamics of carbon dioxide and carbon dioxide cation are thoroughly studied.^{1,7-29} Nevertheless, their photoreactivity in the gas phase and at catalytic interfaces remains an area of active research mainly due to its environmental and technological relevance. For example, UV light ultimately destroys CO_2 with a unit quantum yield. This reaction provides a one-step route towards CO_2 reduction to carbon monoxide³⁰ and is in scope of studies on the negative emission technologies.³¹⁻³³ From a broader perspective, carbon dioxide excited with energetic (UV/VUV/XUV) photons undergoes a series of fundamental photochemical processes typical of highly energy loaded molecular systems. These include non-adiabatic interactions between Rydberg and valence electronic states,²⁸ roaming dissociation pathways leading to unusual photochemical products,^{24,34} or dissociative VUV photoionization.³⁵ Understanding the atomistic and electronic mechanisms of these processes enhances our ability to address the current major technological and climate challenges at the molecular level.

The rapidly expanding field of attochemistry, utilizing the generation of ultrashort attosecond-scale XUV pulses, interrogates the photochemical processes on the time scale typical for the motion of valence electrons. Various spectroscopic and time-resolved pump-probe techniques have emerged, including attosecond spectroscopy³⁶⁻³⁹ and streaking,^{40,41} 2D correlation spectroscopy,^{29,42} and Raman scattering spectroscopy.⁴³ The choice of the particular method is primarily dictated by the nature of the attosecond dynamics one intends to study. Attosecond nonlinear Fourier Transform (NFT) spectroscopy in XUV is an experimental attosecond method which can be directly applied to the investigation of super-excited ionizing and dissociating molecular systems.⁴⁴⁻⁴⁶ With this technique, one detects ions resulting from the coherent interaction between two attosecond pulse trains (APTs) and a molecule excited and ionized via multi-photon transitions. The spectral content of the APTs produced through high-harmonic generation⁴⁷ is commonly limited to odd

harmonics of the fundamental driving frequency ω_0 (usually in the infrared). Figure 1(a) provides examples of the intensity distributions of the harmonics in the APTs used in this work. The two APTs propagate along two interferometric arms with variable delay τ and are focused on the interaction region containing only the molecular species of interest. The NFT spectroscopy is an attosecond pump-probe detection scheme, with identical pump and probe APT pulses. The time delay increments in this technique, determined by the reproducibility with which one can move the interferometric arms and control the relative delay, is in the latest experiments of the order or better than 10 as.⁴⁸ The frequency resolution in the NFT spectroscopy is limited in principle by the maximum delay τ_{\max} of the interferometer, typically of a few femtoseconds,^{46,49} which corresponds to ~ 1 eV. The excitation energy resolution, determined by the width of the temporal envelope of the APTs, is also of the order of 1 eV [cf. Fig. 1(b)].

Attosecond NFT spectroscopy has the potential to provide new information on the dynamics of photodissociation of CO_2 and CO_2^+ .^{45,46} The nonlinear response of CO_2 to APT fields is encoded in the interferometric autocorrelator employing velocity map imaging (VMI), which detects the signals corresponding to the fragment ions, such as C^+ , O^+ , CO^+ , as functions of the time delay τ between the two APTs. For each fragment ion type, the signal of an electron/ion time-of-flight spectrometer such as VMI is rendered⁵⁰ as a two-dimensional (2D) autocorrelation map giving the fragment kinetic energy distribution for each time delay τ . The 2D NFT spectrum, showing the intensity as a function of the kinetic energy and the NFT frequency ω_{NFT} , is obtained by a Fourier transform from the τ domain to the ω_{NFT} domain. Integration over the kinetic energy of the ionic fragment gives a one-dimensional (1D) NFT spectrum representing the total ionic yield as a function of ω_{NFT} and proportional to the total population of the electronic states of the ionized molecule dissociating into the channels containing detected fragments.

The goal of this work is to explore the quantum mechanical aspects of the experimental NFT spectroscopic technique, to construct a theoretical ab initio model for calculation of the NFT spectra of carbon dioxide, and to identify the NFT spectral features which can carry information on the chemical rearrangements within the molecule or the cation. This study provides transparent theoretical means to predict ab initio NFT spectra of small polyatomic molecules with a modest computational effort. We hope that these results can be used to support and to inspire new experimental campaigns.

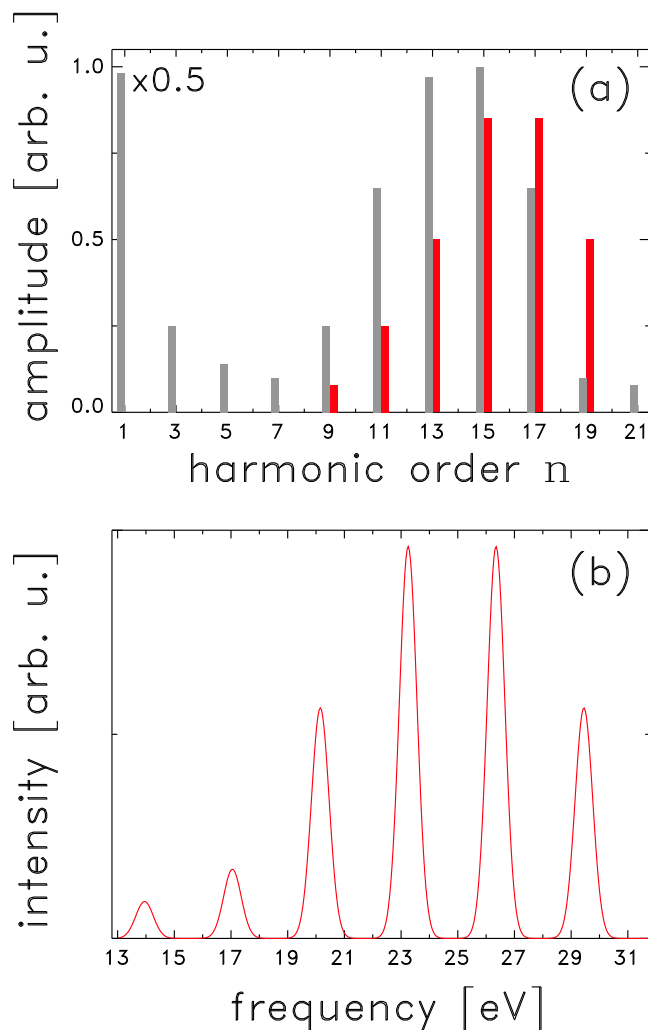


FIG. 1: (a) Amplitudes a_n of the harmonics making up the APTs used in the calculations [cf. Eq. (7)]. Red rectangles: Amplitude Set 1 with only harmonics between $n = 9$ and $n = 19$ included. Grey rectangles: Amplitude Set 2 modeling the experiment of Ref. 46, but with the harmonic amplitude for $n = 1$ strongly amplified to the value of 2. (b) The frequency spectrum of one of the APTs in the calculations. The fundamental frequency of $\omega_0 = 1.55$ eV and the amplitude Set 1 [red rectangles in panel (a)] are used. The temporal width of the APT envelope is 5 fs, giving the spectral width of the harmonic lines of about 0.80 eV.

In what follows, we concentrate on the simplest type of the pump-probe signal — the total ionic yield after two APTs and the associated 1D NFT spectra. The extension to 2D spectra is considered in a separate publication, although we briefly summarize our approach in appendix A. The quantum mechanical description of NFT spectra can be conveniently based on the general framework, developed by Seel and Domcke^{51,52} for two-pulse time

resolved ultrafast ionization spectroscopy of polyatomic molecules. The laser radiation field is treated classically. The interaction between molecule or cation and light is accounted for using the time dependent perturbation theory. The ladder of electronic states of CO_2^+ is computed using high level electronic structure theory including electron correlation.

The analysis of the theoretical NFT spectra of carbon dioxide enables one to evaluate NFT spectroscopy as a research tool and to discuss the following questions: (1) How to assign spectral peaks in 1D NFT spectra? (2) Under which circumstances spectral peaks at non-harmonic NFT frequencies can develop and what is their significance? (3) How sensitive are NFT spectra to variations in the fundamental laser frequency ω_0 ?

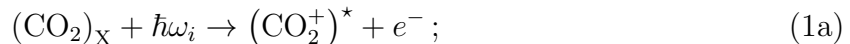
The paper is organized as follows: The quantum mechanical approach to NFT spectra is outlined in Sect. II. This section describes the physical and chemical aspects of the APT-induced photoionization of CO_2 , summarizes the main simplifying assumptions, introduces the Hamiltonian for the system consisting of the molecule and cation interacting with the laser light, and relates the 1D NFT spectrum to the solution of the time dependent Schrödinger equation. The ab initio quantum chemical calculations of the molecular and ionic electronic states are discussed in Sect. III A. The NFT spectra of CO_2 are presented in Sect. III B and compared with the available experimental data. The calculated spectra are assigned in terms of the participating electronic states and the harmonic orders involved in electronic transitions in Sect. III C. Section IV concludes and provides an outlook on the applications of the developed theory, illustrating how the dependence of the NFT spectra on the control parameters can be visualized. Two appendices provide additional information. In Appendix A, the main equations extending the developed theory to 2D spectra are derived. In Appendix B, approximate analytical expressions which support and guide the assignment of the NFT spectra are presented.

II. QUANTUM MECHANICAL APPROACH TO NFT SIGNALS

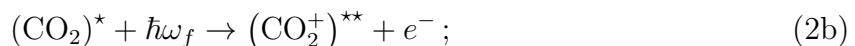
A. The photochemical model

The APT pulses interact with the parent molecule and trigger photoionization and photodissociation reactions. One can broadly distinguish two major photoreaction pathways. In the first one, the parent molecule $(\text{CO}_2)_X$ in the ground electronic state $\tilde{X}^1\Sigma_g^+$ absorbs

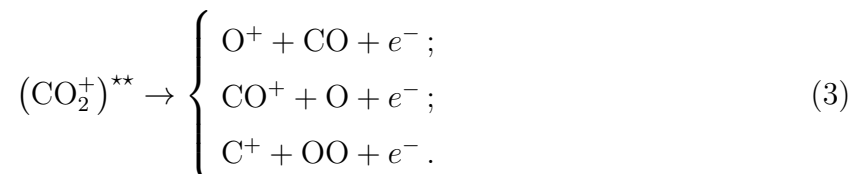
a photon with frequency ω_i and becomes ionized to form cation $(\text{CO}_2^+)^*$, which is further excited with a photon ω_f into dissociative state(s) $(\text{CO}_2^+)^{**}$:



In the second pathway, the parent molecule is promoted into an electronically excited neutral state before ionization:



This pathway is akin to the one explored recently by Adachi et al. in the experimental study of the ultrafast ionization spectroscopy of CO_2 .²⁸ An overview of the neutral and ionic electronic states mediating different photoreaction pathways is given in Fig. 2. The photoexcitations via Eq. (1) are shown with brown arrows and via Eq. (2) — with dark blue arrows. In either pathway, the unstable cation $(\text{CO}_2^+)^{**}$ dissociates into the arrangement channels containing fragment ions, for example O^+ , CO^+ , or C^+ :



The fragment ions are ultimately detected using VMI. The dissociation threshold relevant for the production of O^+/CO^+ fragment ions is close to 19.0 eV (see Ref. 53 and Fig. 2 in which thresholds for various O^+/CO and O/CO^+ channels are marked on the energy scale above the ground state of the neutral CO_2). The appearance of C^+ ions is established to occur between 25.0 eV and 30.0 eV and is attributed to the 3-body dissociation,^{53,54} in Fig. 2, the $\text{C}^+/\text{O}/\text{O}$ channel is located close to 25 eV. As an aside, we note that recent experiments of Lu et al. demonstrated that CO_2 can decompose into the 2-body channel C and O_2 .²⁴ This might suggest that a similar 2-body arrangement channel C^+/O_2 , lying upwards of 17.0 eV, could be detected, too. However, we found no published experimental result so far.

The two-photon excitations in these reactions can be either concerted or sequential. General expressions for the NFT signals, discussed in Sects. IIC and IID, account for both

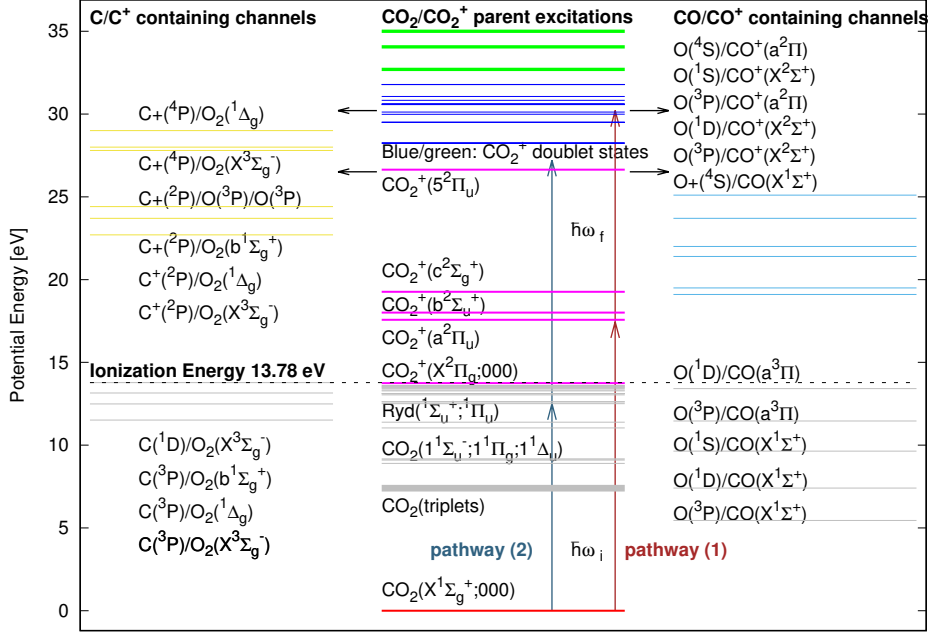


FIG. 2: An overview of ab initio electronic spectra of CO_2 (mainly singlet states) and CO_2^+ (doublet states). The ground electronic state of CO_2 and the electronic states of CO_2^+ are calculated in this work and used in the quantum mechanical NFT spectral calculations. The excited electronic states of CO_2 , shown with gray color, are taken from Refs. 28 and 33. The known two-body dissociation channels of CO_2 and CO_2^+ , with dissociation products and their electronic states. Brown arrows illustrate photochemical pathway of Eq. (1); dark blue arrows — photochemical pathway of Eq. (2). Black arrows indicate dissociations in the electronic states of CO_2^+ .

pathways. The ab initio model in Sect. III A is constructed for the reactions of Eqs. (1) and (3) which constitute the relevant pathway under the experimental conditions of Ref. 46.

The above reaction schemes illustrate the main assumptions made in this work:

A1. Excitations in the Franck-Condon zone only. Equations (1) and (2) imply that all interactions with photons take place in the Franck-Condon zone, before either the neutral CO_2 or the cation CO_2^+ start to decompose. This assumption is justified: Both the APT durations and the pump probe delay times in the NFT experiments are smaller than 10 fs^{45,46} and are therefore substantially shorter than the characteristic times of vibrational motion in CO_2 or CO_2^+ . Judging by the resonance lifetimes of $\sim 50 - 100$ fs calculated for CO_2 ,^{19,22} the dissociation reactions are expected to unfold on a much longer time scale. This has

two implications: First, the ionization of the neutral dissociation fragments, such as CO, O, or C, makes no contribution to the observed NFT signal and can be ignored. Second, the electronic states contributing to the total ion yield (or the 1D NFT spectrum), as well as the transition matrix elements between them, can be found from the quantum chemical calculations limited to the Franck-Condon zone. This simplification is used in Sect. III A to set up the ab initio model.

A2. Single ionizations only. The reaction schemes in Eqs. (1) and (2) involves only single ionizations. Double ionization of carbon dioxide is also possible and has been extensively investigated.^{54–57} The cross section grows with energy in excess of threshold located 37.3 eV above minimum of CO₂. However, the ratio of CO₂²⁺ to CO₂⁺ does not exceed 2% even 30 eV above threshold,^{54,55} and can be neglected in experiments operating APTs with sum frequencies below 70 eV or so. This assumption is also consistent with the mass spectroscopic measurements of Ref. 46 which indicate very low intensities for peaks corresponding to the doubly ionized species.

A3. Two-photon processes only. The reactions in Eqs. (1) and (2) consume only two photons. This is in line with the second order perturbation theory in the molecule-light interaction which we use to find the time dependent excitation and ionization amplitudes. The perturbation theory is known to be reliable for ultrashort laser pulses.⁵⁸ The role of higher order processes in the NFT spectroscopy of CO₂ was discussed,⁴⁶ but no conclusive evidence was found so far. An extension to nonperturbative treatment of excitations and ionizations can be made (see, for example, Ref. 51), but is outside the scope of this work.

With these assumptions, we seek to develop a minimum theoretical description adequate for a quantitative analysis of experimental 1D NFT spectra of photoionizing small polyatomic molecules — taking CO₂ as an example.

B. The Hamiltonian

Quantum mechanical theory of NFT spectra in the setup involving ultrafast time resolved ionization of polyatomic molecules is based on the approach developed in the seminal papers by Seel and Domcke.^{51,52} The electronic basis includes the ground electronic state $|\phi_0\rangle$ of CO₂; a set of excited electronic states of neutral CO₂, $\{|\phi_\alpha\rangle\}$; the one-electron continuum states $|\psi_k^e\rangle$, corresponding to the photoelectron kinetic energy E_k ; and a set of ion core states

$\{|\phi_j^+\rangle\}$ of CO_2^+ . Direct products $|\phi_j^+\psi_k^e\rangle$ define the ionization continua in the model.⁵⁹ The choice of the electronic basis is governed by the assumption **A2** of Sect. II A — only single ionizations are considered.

The molecular Hamiltonian in this basis has the following form:

$$H_M = |\phi_0\rangle H_0 \langle \phi_0| + \sum_{\alpha} |\phi_{\alpha}\rangle H_{\alpha} \langle \phi_{\alpha}| + \sum_j \int_0^{\infty} dE_k |\phi_j^+\psi_k^e\rangle (H_j + E_k) \langle \phi_j^+\psi_k^e|. \quad (4)$$

The electronic basis states, both neutral and ionic, are treated as diabatic. Possible non-adiabatic off-diagonal interactions between them are suppressed and will be explicitly considered in a separate publication on 2D NFT spectra.

The Hamiltonians H_0 , H_{α} , and H_j describe the vibrational dynamics in the electronic ground state of CO_2 , in the excited electronic states of CO_2 , and in the electronic states of CO_2^+ , respectively. Vibrational eigenstates in each electronic state are given by:

$$\begin{aligned} H_0|0\rangle &= \epsilon_0|0\rangle; \\ H_{\alpha}|v_{\alpha}\rangle &= \epsilon_{v_{\alpha}}|v_{\alpha}\rangle; \\ H_j|v_j\rangle &= \epsilon_{v_j}|v_j\rangle; \end{aligned}$$

The vibrational energies $\epsilon_{v_{\alpha}}$ and ϵ_{v_j} are measured with respect to the energy ϵ_0 of the ground vibrational state in the state $\tilde{X}^1\Sigma_g^+$ of CO_2 . For example, the energy $\epsilon_{v_j=1}$ of the ground vibrational state in the ground electronic state $\tilde{X}^2\Pi_g$ of CO_2^+ is approximately equal to 13.8 eV, the ionization energy of CO_2 [cf. Fig. 2].

The external electric field $\mathcal{E}(t)$ is comprised of two APT fields, one of which is delayed by a time τ :

$$\mathcal{E}(t) = \mathcal{E}_{\text{APT}}(t, 0) + \mathcal{E}_{\text{APT}}(t, \tau). \quad (5)$$

The time profile of each APT field is determined by the envelope function $L_n(t, \tau)$:⁴⁶

$$\mathcal{E}_{\text{APT}}(t, \tau) = \sum_{n=n_1}^{n_2} ' a_n L_n(t, \tau) e^{-i\omega_n(t-\tau)}. \quad (6)$$

Here n is the harmonic order (the primed sum runs only over odd orders); ω_n are the harmonic frequencies; a_n is the amplitude of the n -th harmonic in the APT. Gaussian time envelope is often considered,

$$L_n(t, \tau) = \left(\frac{P}{\pi}\right)^{1/2} \frac{1}{T} e^{-P(t-\tau)^2/T^2}, \quad (7)$$

and will be used in the numerical calculations in this work. In this expression, T is the FWHM of the APT Gaussian envelope and $P = 4 \ln 2$. The pump-probe time delay τ is the time interval between the centers of the Gaussian envelopes of the two APTs. The APT spectral shape for the pulse of an experimentally realistic⁴⁶ duration of $T = 5$ fs is shown in Fig. 1(b). The widths of the individual harmonic peaks are slightly below 1 eV and therefore are comparable to the fundamental frequency ω_0 (which is 1.55 eV in the figure).

The interaction between the molecule and the external electric field $\mathcal{E}(t)$ includes the following components capable of describing the pump-probe dynamics along the photoreaction pathways of Eqs. (1) and (2):⁶⁰

1. **Photoreaction pathway of Eq. (1).** The interaction term describing this pathway comprises two components:

$$W_1(t) = W_{1A}(t) + W_{1B}(t). \quad (8)$$

with one of them mediating ionization out of the ground state of CO₂,

$$W_{1A}(t) = - \sum_i \int_0^\infty d E_k |\phi_i^+ \psi_k^e\rangle \mu_{i0}(E_k) \mathcal{E}(t) \langle \phi_0 | + h.c., \quad (9)$$

and the other allowing optical excitations between states of the free ionic core:

$$W_{1B}(t) = - \sum_{i,j \neq i} |\phi_j^+\rangle \mu_{ji} \mathcal{E}(t) \langle \phi_i^+ | \int_0^\infty d E_k |\psi_k^e\rangle \langle \psi_k^e | + h.c. \quad (10)$$

In these expressions, $\mu_{i0}(E_k)$ is the ionization dipole moment, and μ_{ji} is a transition dipole moment (TDM) between ionic states j and i .

2. **Photoreaction pathway of Eq. (2).** The interaction term is structurally similar to the above:

$$W_2(t) = W_{2A}(t) + W_{2B}(t), \quad (11)$$

with one term describing optical excitations in the neutral molecule,

$$W_{2A}(t) = - \sum_\alpha |\phi_\alpha\rangle \mu_{\alpha 0} \mathcal{E}(t) \langle \phi_0 | + h.c., \quad (12)$$

and the other giving rise to the ionization from the state $|\phi_\alpha\rangle$ of CO₂:

$$W_{2B}(t) = - \sum_{j\alpha} \int_0^\infty d E_k |\phi_j^+ \psi_k^e\rangle \mu_{j\alpha}(E_k) \mathcal{E}(t) \langle \phi_\alpha | + h.c.. \quad (13)$$

Here $\mu_{\alpha 0}$ are the TDMs for optical excitations in the neutral CO_2 from the ground electronic state $\tilde{X}^1\Sigma_g^+$, and the ionization dipole moments $\mu_{j\alpha}(E_k)$ are now defined for a given pair of the ionic state j and the neutral state α .

The total Hamiltonian governing the dynamics in the time dependent electric field $\mathcal{E}(t)$ is given by the sum of the molecular Hamiltonian [Eq. (4)] and the interaction with laser field:

$$H_{TOT}(t) = H_M + W_1(t) + W_2(t). \quad (14)$$

The TDMs between diabatic states are treated in the Condon approximation consistent with the diabatic representation. For the ionization step, the dipole moments $\mu_{i0}(E_k)$ and $\mu_{j\alpha}(E_k)$ depend on the photoelectron kinetic energy E_k and are subject to the boundary condition $\mu(E_k) \rightarrow 0$ as $E_k \rightarrow \infty$. Following Seel and Domcke,⁵¹ we approximate this dependence by a simple step function, e.g.

$$\mu_{i0}(E_k) = \begin{cases} \mu_{i0}, & \text{if } 0 \leq E_k \leq E_k^{\max} \\ 0, & \text{if } E_k > E_k^{\max} \end{cases} \quad (15)$$

The cutoff energy E_k^{\max} is a parameter of the calculation controlling the width of the photoelectron spectrum in a given ionic state.

C. NFT signals

The NFT signal calculated in this work is the total yield $I_{\text{ion}}(\tau)$ of the detected fragment ion [for example, C^+ , O^+ , or CO^+ , cf. Eq. (3)]. This 1D signal is proportional to the total population of the ionic electronic states dissociating to produce the detected ion. The ladder model in Fig. 2, approximating the electronic spectrum of CO_2^+ with ab initio energies at the Franck-Condon point, can be taken as a starting point for a calculation of $I_{\text{ion}}(\tau)$. After the pump and probe pulses, the system, consisting of CO_2^+ and a photoelectron, is left in the state $\Psi_I(t|E_k, \tau)$. The population p_f of a dissociative final state $|f\rangle$ of CO_2^+ is given by

$$p_f(E_k, \tau) = |\langle \phi_f^+ \psi_k^e | \Psi_I(t \rightarrow \infty | E_k, \tau) \rangle|^2. \quad (16)$$

The total ion yield $I_{\text{ion}}(\tau)$ is proportional to this population integrated over the photoelectron kinetic energy E_k and summed over all final states having energies ϵ_f above the appearance

threshold A_{ion} of the detected ion:

$$I_{\text{ion}}(\tau) = \sum_{f: \epsilon_f > A_{\text{ion}}} \int_0^\infty dE_k p_f(E_k, \tau). \quad (17)$$

Fourier transform of $I_{\text{ion}}(\tau)$ gives the frequency domain 1D NFT spectrum:

$$I_{\text{ion}}(\omega_{\text{NFT}}) = \int_{-\tau_{\text{max}}}^{\tau_{\text{max}}} d\tau I_{\text{ion}}(\tau) e^{i\omega_{\text{NFT}}\tau} \quad (18)$$

The maximum time delay τ_{max} defines the spectral resolution in the NFT frequency ω_{NFT} .

NFT signals of CO_2 are also reported as 2D maps $I_{\text{ion}}(\epsilon_{\text{kin}}, \tau)$, in which the kinetic energy distribution of the recoiling fragment ions is measured for different time delays. The NFT observable in this case is directly related to the dissociation dynamics in the ionic states, and the description of the signal requires basic elements of scattering theory. The scattering approach to the 2D NFT signals is outlined in Appendix A. Numerical applications are considered in a separate publication.

D. Total ion yield via time dependent perturbation theory

Evaluation of the NFT signals described with Eqs. (16) and (17), as well as with Eqs. (A3) and (A5), requires the time dependent molecular wave function $|\Psi_I(t; E_k, \tau)\rangle$ in the interaction representation. We expand it in the electronic basis introduced in Sect. II B:

$$|\Psi_I(t; E_k, \tau)\rangle = \chi_0(t) |\phi_0\rangle + \sum_{\alpha} \chi_{\alpha}(t) |\phi_{\alpha}\rangle + \sum_j \int_0^\infty dE_k \chi_j(t; E_k, \tau) |\phi_j^+ \psi_k^e\rangle, \quad (19)$$

Here the coefficients $\chi_0(t)$ and $\chi_{\alpha}(t)$ are the nuclear wave functions in the ground (index 0) and excited (indices α) electronic states of the neutral molecule; $\chi_j(t; E_k, \tau)$ are the nuclear wave functions of the molecular ion depending on the photoelectron kinetic energy E_k and, through the APT fields, on the pump probe time delay τ . The initial state of the molecule is assumed to be the vibrational ground state in the electronic ground state, $|\phi_0\rangle |0\rangle$.

The coefficient $\chi_j^{(2)}(t; E_k, \tau)$ for the CO_2^+ ion in one of the final dissociative states is evaluated using the second order time dependent perturbation theory in the interactions $W_1(t)$ and $W_2(t)$. This is in line with the assumption **A3** of Sect. II A, so that the theoretical description focuses on the two-photon processes. Perturbation theory allows us to concentrate on the observable ion signal and bypass a rigorous description of the ejected electron which

has not been detected in the NFT spectroscopic experiments on CO₂. In fact, the photoelectron dynamics is very rich in carbon dioxide,⁶¹ and was a subject of detailed theoretical and experimental studies on the attosecond time scale.^{27,29}

The contributions of the interactions with laser fields to the wave functions (and to the pump probe amplitudes) are additive. Considering the interaction $W_1(t)$, the second order nuclear wave function is given by:

$$\chi_j^{(2)}(t; E_k, \tau) = \frac{1}{i^2} \sum_{i \neq j} \int_{-\infty}^t dt_1 \int_{-\infty}^{t_1} dt_0 e^{iH_j t_1} [\mu_{ji} \mathcal{E}(t_1)] e^{iE_k t_0} e^{-iH_i(t_1-t_0)} [\mu_{i0}(E_k) \mathcal{E}(t_0)] e^{iH_0 t_0} |0\rangle. \quad (20)$$

We use $\hbar = 1$ throughout the paper. The amplitude $\chi_j^{(2)}$ describes ionization of the molecule in the vibrationless ground state $|0\rangle$ into an ionic state i at time t_0 , and a subsequent optical excitation of the state i into the final state j at time t_1 [photoreaction via the Eq. (1)]. The pump probe experiment is represented as a linear combination of photoionization/excitation events separated by the temporal delay of length τ . Projecting this function onto the final vibrational state $\langle v_j |$ and taking the limit $t \rightarrow \infty$ gives the asymptotic second order pump probe amplitude due to the interaction $W_1(t)$:

$$c_j(v_j; E_k, \tau) = \frac{1}{i^2} \sum_{i \neq j} \sum_{vi} \mu_{ji} \langle v_j | v_i \rangle \mu_{i0}(E_k) \langle v_i | 0 \rangle \times \int_{-\infty}^{\infty} dt_1 e^{i(\epsilon_{vj} - \epsilon_0 + E_k)t_1} \mathcal{E}(t_1) \int_{-\infty}^{t_1} dt_0 e^{-i(\epsilon_{vi} - \epsilon_0 + E_k)(t_1 - t_0)} \mathcal{E}(t_0). \quad (21)$$

The pump probe amplitudes $c_j(v_j; E_k, \tau)$ depend on the time delay τ via the time dependence of the laser field $\mathcal{E}(t)$, cf. Eqs. (5) and Eqs. (6) and (7). The coefficients $\langle v_i | 0 \rangle$ in Eq. (21) are the expansion coefficients of the initial vibrational state $|0\rangle$ in the vibrational states of the intermediate ionic states, $|v_i\rangle$; the coefficients $\langle v_j | v_i \rangle$ are the projections of the intermediate ionic vibrational states onto the final state $|v_j\rangle$.

Repeating the same steps for the interaction $W_2(t)$, one finds another contribution to the pump probe amplitude due to an optical excitation of the molecule in the vibrationless ground state $|0\rangle$ into a neutral state α at time t_0 , and a subsequent ionization of the state α into the final state j at time t_1 [photoreaction via the Eq. (2)]:

$$d_j(E_k, v_j, \tau) = \frac{1}{i^2} \sum_{\alpha > 0} \sum_{v\alpha} \mu_{j\alpha}(E_k) \langle v_j | v_\alpha \rangle \mu_{\alpha 0} \langle v_\alpha | 0 \rangle \times \int_{-\infty}^{\infty} dt_1 e^{i(\epsilon_{vj} - \epsilon_0 + E_k)t_1} \mathcal{E}(t_1) \int_{-\infty}^{t_1} dt_0 e^{-i(\epsilon_{v\alpha} - \epsilon_0)(t_1 - t_0)} \mathcal{E}(t_0). \quad (22)$$

The coefficients $\langle v_\alpha|0\rangle$ and $\langle v_j|v_\alpha\rangle$ in this equation are similar to the respective coefficients in Eq. (21), but refer to the projections of the vibrational states in the excited electronic states of the neutral molecule. The total pump probe amplitude $b_j(E_k, v_j, \tau)$ is given by the sum of the amplitudes for the two pathways:

$$b_j(E_k, v_j, \tau) = c_j(E_k, v_j, \tau) + d_j(E_k, v_j, \tau) \quad (23)$$

The ionic signal $I_{\text{ion}}(\tau)$, defined in the Eq. (17), is proportional to the population p_f in the final dissociative states $|f\rangle$ capable of producing the detected ion, i.e. to the square of the pump probe amplitudes $|b_f|^2$ collected over vibronic levels ϵ_{vf} lying above the appearance threshold A_{ion} :

$$I_{\text{ion}}(\tau) = \sum_f \sum_{\epsilon_{vf} > A_{\text{ion}}} \int_0^\infty dE_k |b_f(E_k, v_f, \tau)|^2. \quad (24)$$

This is a working expression in the calculations discussed in Sect. III. It is valid even if different electronic states interact non-adiabatically⁶² — the vibronic energies ϵ_{vf} in this case should refer to adiabatic rovibronic eigenstates.

III. RESULTS AND DISCUSSION

A. Ab initio calculations of CO_2 and CO_2^+

The challenge in modeling NFT spectra for polyatomics is to construct an adequate (preferably ab initio) model of electronic states of the neutral molecule and the molecular ion. Strictly speaking, potential energy surfaces depending on all three internal coordinates are needed to find the eigenstates ϵ_{vj} and to calculate even the total ion yield. Due to a multiphoton nature of the NFT technique and the XUV harmonics used for excitation and ionization, this can easily become a formidable task because tens or even hundreds (interacting) electronic states might be needed.²⁸

In this work, we use the assumption **A1** of Sect. II A and calculate the electronic energy levels, as well as the dipole moments for the ionization and optical excitation steps, at the equilibrium geometry of the ground electronic state of the neutral molecule. The symmetry group of this Franck-Condon point is $D_{\infty h}$. In the electronic structure calculations, it is rendered as D_{2h} .

The ab initio calculations are further simplified by concentrating the analysis on the photoreaction pathway of Eq. (1), so that ionizations take place directly from the ground electronic state of CO₂. This relieves us of having to calculate the densely spaced mixed Rydberg-valence states of the neutral molecule close to the ionization threshold.²⁸ The photoreaction pathway of Eq. (1) is indeed likely to make the main contribution to the observed NFT signals of CO₂.⁴⁶ Carbon dioxide is transparent up to about 6.20 eV (where the absorption still remains extremely weak),^{63–65} and the first strong absorption band is observed near 11.08 eV.^{10,66} The molecule ionizes at 13.8 eV, while the harmonics which substantially contribute to the APTs considered in the present calculations carry excitation energies of more than 14.0 eV [cf. Fig. 1(b)]. Possible spectral signatures of the complementary pathway of Eq. (2) will be indicated in the discussion of the results.

The augmented correlation consistent polarized valence quadrupole zeta (aug-cc-pVQZ) basis set due to Dunning is used for all atoms. Energies of CO₂ and CO₂⁺ are calculated at the internally-contracted multireference configuration interaction singles and doubles (MRD-CI) level, based on state-averaged full-valence complete active space self-consistent field (CASSCF) calculations with 16 electrons in 12 active orbitals and 6 electrons in three fully optimized closed-shell inner orbitals. Active space in CASSCF comprises orbitals $2\sigma_u - 4\sigma_u$, $3\sigma_g - 5\sigma_g$, $1\pi_u - 2\pi_u$, and $1\pi_g$. In the MRD-CI step, all 16 valence electrons are correlated. The Davidson correction is applied in order to account for higher-level excitations and size extensivity. The singlet ground electronic state of CO₂ and a series of doublet states of CO₂⁺ are calculated with this setup. The MRD-CI calculations for the ion are performed using the molecular orbitals of the neutral molecule in order to simplify the evaluation of ionization matrix elements. All ab initio calculations are carried out with the MOLPRO package.^{67,68}

More than 50 doublet electronic states of CO₂⁺ are calculated and assigned. The full list of converged states includes $1 - 4^2\Sigma_g^+$; $1 - 7^2\Sigma_u^+$; $1 - 6^2\Sigma_g^-$; $1 - 6^2\Sigma_u^-$; $1 - 10^2\Pi_g$; $1 - 10^2\Pi_u$; $1 - 4^2\Delta_g$; and $1 - 4^2\Delta_u$. These states span the energy range from 13.8 eV to 32.5 eV above the minimum of the ground electronic state of the neutral CO₂ molecule.

The ionization dipole moments μ_{i0} between the states of CO₂⁺ and the ground electronic state of CO₂ are evaluated for the CI vectors calculated in the common basis of the molecular orbitals of the neutral CO₂. For a given ionic state i , the photoionization dipole moment

μ_{i0} reads as

$$\mu_{i0} = \sum_s d_{ks}(E_k) x_{i0}^s. \quad (25)$$

It is a sum of products of bound-free one-electron dipole integrals $d_{ks}(E_k)$ which depend on the photoelectron kinetic energy E_k , and the ‘spectroscopic factors’ x_{i0}^s defined as⁶⁹

$$x_{i0}^s = \langle \phi_i | \hat{c}_s | \tilde{X}^1 \Sigma_g^+ \rangle. \quad (26)$$

where \hat{c}_s stands for the annihilation operator for the orbital s , and ϕ_i is the electronic wave function of the cation state i . The spectroscopic factors are calculated for the CI vectors of CO_2 and CO_2^+ using the algorithm proposed by W. Einfeld.⁷⁰ Note that spin selection rules are relaxed in photoionization, and higher multiplicity spin states of CO_2^+ (e.g. quartets) can in principle be ionized, too. Test calculations performed for the four lowest quartet states $1, 2^4A'$ and $1, 2^4A''$ demonstrate, however, that the spectroscopic factors for these ionizations are small.

Optical transitions between the states of the ion require interstate TDMs μ_{ji} . Components (μ_x, μ_y, μ_z) of the TDM vector are calculated at the high symmetry Franck-Condon point. The coordinate axes in these calculations are chosen such that z runs along the molecular figure axis, while x and y are orthogonal to z . The ab initio TDMs are computed at the CASSCF level of theory. Previous calculations demonstrate²¹ that the difference between the TDMs calculated using CASSCF and MRD-CI methods is less than 10%.

At the high symmetry Franck-Condon geometry, the selection rules effectively reduce the number of accessible optically bright states; for many pairs of symmetry species, the x , y , and z components of the TDMs μ_{ji} vanish. For example, for the five states $1^2\Pi_g$, $1^2\Pi_u$, $1^2\Sigma_u^+$, $1^2\Sigma_g^+$, and $5^2\Pi_u$ (they have the largest photoionization probabilities), the optical transitions are driven by very few non-zero TDM components:

$$\begin{pmatrix} 1^2 \Pi_g & \mu_z & \mu_{x,y} & - & \mu_z \\ & 1^2 \Pi_u & - & - & - \\ & & 1^2 \Sigma_u^+ & \mu_z & - \\ & & & 1^2 \Sigma_g^+ & - \\ & & & & 5^2 \Pi_u \end{pmatrix} \quad (27)$$

In this symbolic representation, the TDM components mediating transitions between states on the main diagonal of the matrix are enumerated as off-diagonal ‘matrix elements’. The resulting ‘matrix’ is sparse.

Consequently, only a subset of all calculated states of CO_2^+ are included in the quantum mechanical calculations of the NFT spectra. This subset is shown in Table I and in Fig. 2. The accuracy of the ab initio calculations can be judged (for the first several states) by comparison with the known experimental energies,⁷¹ also shown in Table I where available. The states of CO_2^+ in Table I are selected as follows: (1) Five states with the largest photoionization probabilities $|\mu_{i0}|^2$ referenced in Eq. (27). They are shown above the upper horizontal line in Table I and as magenta lines in Fig. 2. (2) Thirteen states having strong ($> 0.2\text{D}$) TDMs with the above 5 preselected ionization states are additionally included in the model. They are shown with blue color in Fig. 2. (3) For several states, assigned $n^2\Sigma_g^+$, $n^2\Pi_u$ and $n^2\Sigma_u^+$ and shown below the lower horizontal line in Table I, convergence at the MRD-CI level was not achieved. Their energies were shifted in the quantum mechanical calculations to the values shown in parenthesis. These states are shown as green lines in Fig. 2. These states collectively represent the electronic states lying outside the energy range covered by the present ab initio calculations.

B. Calculated and experimental NFT spectra

The NFT signals are calculated using Eqs. (18) and (24), and only the pump probe amplitude $c_j(E_k, \nu_f, \tau)$ of Eq. (21) is included. The vibrational excitations are suppressed for all states, so that each electronic state contributes one energy ϵ_{0j} coinciding with the ab initio energy for this state in Table I.

It is assumed that ions in Eqs. (3) are produced with the appearance thresholds of $A_{\text{C}^+} = 30.0\text{eV}$ and $A_{\text{O}^+} = A_{\text{CO}^+} = 19.0\text{eV}$. All electronic states with energies above the appearance threshold A_{ion} contribute to the fragment ion generation. As explained in Sect. II A, the appearance thresholds for O^+ and CO^+ are close to the known channel dissociation thresholds shown in Fig. 2, while A_{C^+} is taken substantially higher than the lowest dissociation energy of 23eV , at which the production of C^+ ions becomes energetically allowed.

Two sets of APTs, shown in Fig. 1(a), are used in the calculations. Set 1 (red boxes) spans the harmonic orders from $n = 9$ to $n = 19$, with a standard choice of harmonic amplitudes of the components.^{72,73} Set 2 covers harmonic orders from $n = 1$ to $n = 21$, as reported for the APTs in Ref. 46. Compared to Set 1, it incorporates contributions from low harmonic

orders $n \leq 7$. We also artificially amplified the amplitude for $n = 1$. Such an amplitude distribution is valuable because it describes realistic experimental conditions under which the fundamental ω_0 or the adjacent odd harmonics are not fully suppressed e.g. by dichroic mirrors, filters, or harmonic separators. The additional change in the amplitude for $n = 1$ on top of the reported amplitudes, helps to rationalize the intensity of this harmonic peak in the measured NFT spectrum.

The ionization transition matrix elements $\mu_{i0}(E_k)$ between the ground electronic state of CO_2 and the first five ionic states in Table I are assumed to be constant up to the maximum cutoff energy E_k^{max} [cf. Eq. (15)], and negligible beyond this energy; E_k^{max} determines the upper integration limit over the electron kinetic energy in Eq. (24). Most calculations in this work are carried out with $E_k^{\text{max}} = 3.0 \text{ eV}$. The dependence of $\mu_{i0}(E_k)$ on E_k stems from the bound-free dipole integrals $d_{ks}(E_k)$ in Eq. (25) and is essentially governed by the overlap of a valence orbital of CO_2 and a distorted plane wave corresponding to the photoelectron ejected with the kinetic energy E_k . This overlap drops with increasing E_k leading to narrow photoelectron spectra of these states, with the measured¹⁵ and calculated⁶¹ electron binding energy widths below 2.0 eV. Broad photoelectron kinetic energy distributions exceeding 7.0 eV, were observed for CO_2 initially pre-excited into the Rydberg states near ionization threshold.²⁸ Additionally, electron kinetic energies up to and exceeding 10 eV were previously measured in the ionization of CO_2 with XUV APTs.^{27,29} In order to assess the role of E_k^{max} , some calculations for Set 1 were repeated with $E_k^{\text{max}} = 10.0 \text{ eV}$. Spectral peaks were reproduced across the full range of ω_{NFT} . The impact of E_k^{max} on the peak intensities was visible only at high NFT frequencies above $13\omega_0$.

An example of the calculated NFT signal $I_{C+}(\tau)$ in the time domain is shown in Fig. 3 for the pump-probe APTs with the amplitude Set 1. The fundamental harmonic frequency is $\omega_0 = 1.55 \text{ eV}$, close to the experimental value used in Ref. 46. The pump probe time delay τ in the calculations varies between $\pm\tau_{\text{max}} = \pm 20 \text{ fs}$. This guarantees a tidy rendering of the NFT spectra in the frequency domain via Eq. (18). The chosen τ_{max} is about three times larger than the experimental value.

In the NFT signal $I_{C+}(\tau)$ in Fig. 3, most of the visible dynamical effects are concentrated within $|\tau| \leq 7 \text{ fs}$, which is about 2–3 times the optical cycle of the fundamental laser frequency. With growing ω_0 , the signal amplitudes are observed to decrease substantially (not shown in Fig. 3). The dependence of the NFT signal intensity on the fundamental laser

frequency is considered in more detail in Sect. IV.

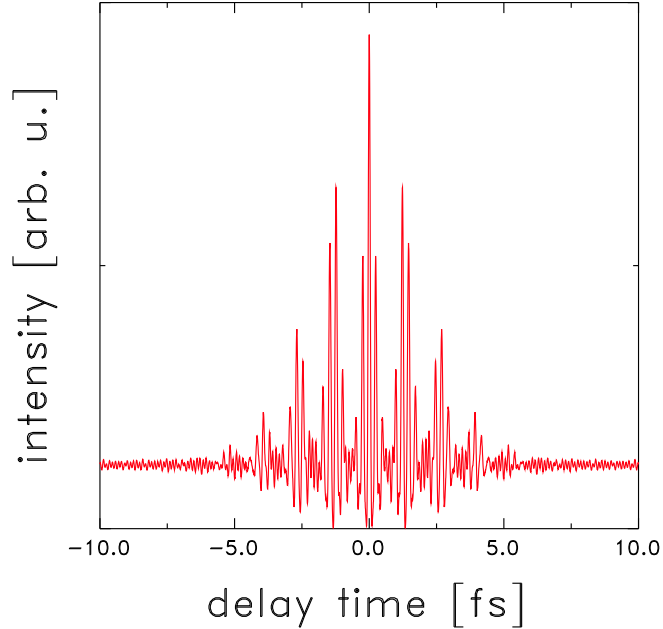


FIG. 3: Ab initio pump probe NFT signal $I_{C+}(\tau)$ in a simulation with the fundamental frequency of $\omega_0 = 1.55$ eV and the amplitude Set 1. The optical cycle of the fundamental laser pulse is $T_0 = 2.67$ fs.

Fourier transform of the signal in Fig. 3 gives the frequency dependent spectrum $I_{C+}(\omega_{\text{NFT}})$ depicted in Fig. 4(a). The calculated spectrum consists of a series of non-overlapping peaks with FWHM of about 0.9 eV, similar to the width of the harmonics making up the pump and probe APTs. In order to simplify visual comparison with the spectral content of the incident APTs, the NFT frequency axis is shown in the units of the fundamental frequency ω_0 . Two groups of spectral peaks can be identified. The first group comprises peaks located sufficiently close to the harmonic orders, either odd, i.e. present in the incident APTs, or even. Example is the strong triad at $\omega_{\text{NFT}} \approx 9\omega_0$, $11\omega_0$, and $13\omega_0$ in panel (a), although the peaks $9\omega_0$ and $11\omega_0$ slightly but visibly deviate from the harmonic position. The assignment of the excitation patterns, discussed in Sect. III C, suggests that this triad is due to (a) ionizations into the the ground electronic state $\tilde{X}^2\Pi_g$ of CO_2^+ , as well as the first excited doublet state $A^2\Pi_u$, and (b) dissociations in the high lying electronic states belonging to the series $n^2\Pi_g$ and $n^2\Pi_u$. Previous analyses of the NFT spectra concentrated mainly on the peaks belonging to this group.⁴⁶ Gradually attenuating contributions of $15\omega_0$, $17\omega_0$, and $19\omega_0$ can also be recognized. However, they lie beyond the detection

range of the experimental setup limited to less than 25.0 eV or $\omega_{\text{NFT}} < 15\omega_0$.⁷⁴ Note that the relative intensities of the harmonic peaks in the NFT spectrum are quite different from those in the incident APT [cf. Set 1 in Fig. 1(a)].

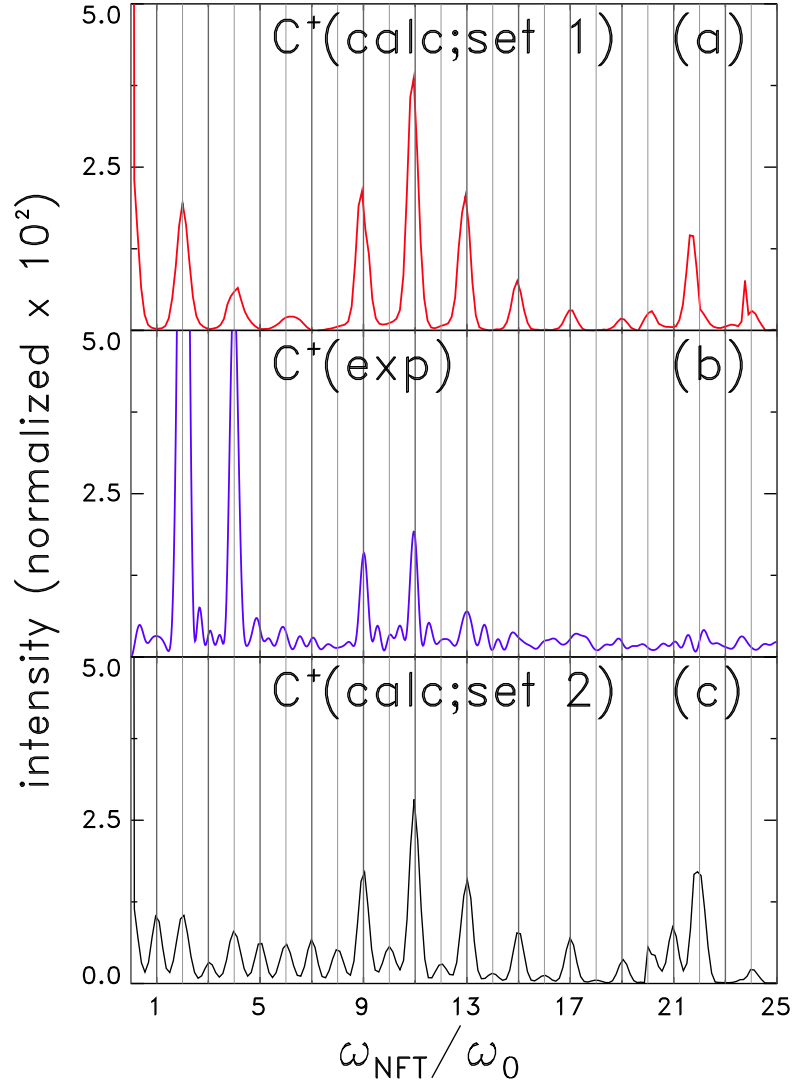


FIG. 4: Ab initio pump probe NFT spectra $I_{C^+}(\omega_{\text{NFT}})$ of CO_2 calculated using APTs with the amplitude Set 1 (a) and Set 2 (c). The fundamental frequency in the calculations is $\omega_0 = 1.55$ eV. Shown in (b) is the 1D NFT spectrum of Ref. 46 obtained from the experimental 2D NFT spectrum for the C^+ fragment in their Fig. 12(c) by integrating over the fragment kinetic energy. All spectra are normalized to the area within the region of $\omega_{\text{NFT}} \leq 25.0$ eV. Thick (thin) vertical lines indicate odd (even) integer harmonic orders $\omega_{\text{NFT}}/\omega_0$.

Another example of peaks in this group are spectral lines at even harmonic orders $2\omega_0$ and $\sim 4\omega_0$. They are absent in the APTs and have been previously attributed to the

frequency beats between the incident odd harmonics.⁴⁶ In other words, they are seen as difference frequency peaks stemming from the ‘parent’ triad e.g. $(13\omega_0 - 11\omega_0)$ for the second harmonic peak and $(13\omega_0 - 9\omega_0)$ for the fourth harmonic peak.

The second group of spectral peaks is formed by the peaks located at non-harmonic frequencies. Examples include the peak between $6\omega_0$ and $7\omega_0$ and, to a lesser extent, the peaks near $\sim 4\omega_0$ and $\sim 9\omega_0$, as well as the high frequency peaks above $20\omega_0$.

The experimental NFT spectrum $I_{C^+}(\omega_{\text{NFT}})$ is shown in Fig. 4(b). It is obtained from the full 2D spectrum published in Ref. 46 by integrating over the kinetic energy axis. One finds peaks belonging to the same two groups discussed above. The triad near $\omega_{\text{NFT}} \approx 9\omega_0$, $11\omega_0$, and $13\omega_0$ is again well recognizable. The difference frequency peaks at $2\omega_0$ and $4\omega_0$ are very strong. This observation is unexpected because the difference peaks turn out to be much stronger than any ‘parent’ harmonic peak in the spectrum. Their intensities in the normalized spectrum are six times stronger than in the calculations. Finally, several non-harmonic peaks are seen in the experimental spectrum, for example between $4\omega_0$ and $6\omega_0$. Note however that the experimental spectrum is quite congested with a low intensity ‘noisy’ contribution covering the whole experimental NFT frequency range.

The amplitude Set 1 does not properly describe the experimental APTs of Ref. 46, because many low frequency harmonic components are missing. The amplitude Set 2, depicted in Fig. 1 with gray boxes, is a better model of this experiment. The artificially amplified amplitude of the fundamental $n = 1$ is immaterial for the case of C^+ ion signal and does not affect the spectrum $I_{C^+}(\omega_{\text{NFT}})$ at all. The spectrum calculated with Set 2 is shown in Fig. 4(c). The low frequency harmonics have no impact on the spectral peaks of the strong triad $9\omega_0 - 11\omega_0 - 13\omega_0$, which are still well recognizable, similarly to the experimental spectrum. The Set 2 adds a substantial low intensity component to the spectrum producing a small spectral peak at every harmonic order n , both even and odd. This feature is also in line with the experiment. Note that the low intensity component is entirely absent in panel (a), so that the ‘noise’ in the calculation stems from the harmonic orders $3 \leq n \leq 7$. Nevertheless, the agreement between the calculated and the measured spectra is at best qualitative, and the relative intensities for many peaks, for example $2\omega_0$ and $4\omega_0$, disagree substantially.

Lowering the appearance threshold from 30.0 eV to 19.0 eV, one can use the same ladder ab initio electronic states to evaluate the NFT spectrum $I_{O^+}(\omega_{\text{NFT}})$ for the fragment ion O^+ . The results are summarized in Fig. 5 for the amplitude Set 1 in panel (a) and Set 2 in

panel (c). The experimental spectrum is shown in panel (b).

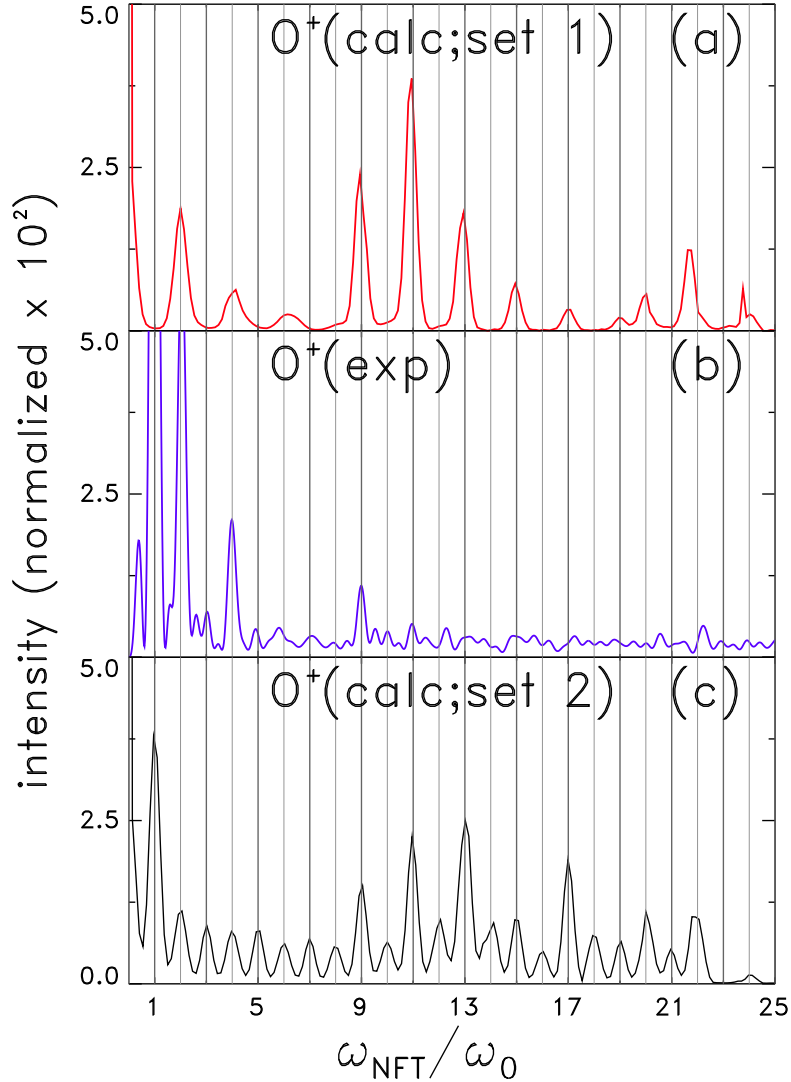


FIG. 5: As in Fig. 4, but for the spectrum $I_{O^+}(\omega_{\text{NFT}})$. The 1D NFT spectrum in panel (b) is obtained from the experimental 2D NFT spectrum of Ref. 46 for the O^+ fragment in their Fig. 13(c) by integrating over the fragment kinetic energy.

The experimental spectra recorded for O^+ and C^+ are similar in several respects. For example, the triad near $9\omega_0 - 11\omega_0 - 13\omega_0$ is still visible in $I_{O^+}(\omega_{\text{NFT}})$ (although the peaks are shifted more clearly to non-harmonic positions), and the low energy peaks at $2\omega_0$ and $4\omega_0$ are strong. However, the experimental spectrum $I_{O^+}(\omega_{\text{NFT}})$ is dominated by the very intense peak $n = 1$ of the fundamental frequency ω_0 . Additionally, there are more non-harmonic peaks in the O^+ spectrum than in the C^+ spectrum, and their intensity is higher.

The amplitude Set 1 is clearly incompatible with experiment: The spectrum in Fig. 5(a)

is almost the same as in Fig. 4(a) and is insensitive to a shift in the appearance threshold. Indeed, the amplitude Set 1 comprises harmonics with energies above 14 eV, so that the high lying states of CO_2^+ are primarily populated along the photochemical pathway of Eq. (1). In the adopted model, these states contribute to both O^+ and C^+ signals.

The O^+ spectrum calculated with Set 2 and shown Fig. 5(c) is different and has a pronounced peak at $\omega_{\text{NFT}}/\omega_0 = 1$. In the C^+ spectrum, calculated with the same Set 2, this peak is much weaker. Low order harmonics in Set 2 induce excitations between neighboring electronic states of CO_2^+ and this directly influences the NFT spectrum. For example, the spacing between the states $1^2\Sigma_u^+$ and $1^2\Sigma_g^+$ is 1.26 eV (see Table I) and is nearly resonant with ω_0 . Still, a single resonant electronic transition in CO_2^+ alone is not sufficient to make the peak $n = 1$ intense: In the calculations, the large amplitude a_1 of the fundamental in the incident APT is also a pre-requisite; the chosen amplitude a_1 exceeds the value inferred from Ref. 46, by about a factor of 20. It is therefore likely that the very strong peak at ω_0 in the experimental spectrum has a different origin missing in the present calculations. One possibility are higher order multiphoton excitations.⁴⁶ The other are contributions from the photochemical pathway of Eq. (2), in which CO_2 is photoexcited into the vicinity of the ionization threshold and then ionized with an infrared photon. Note that the reversed order of absorptions would be unfeasible because CO_2 is essentially transparent around 1.55 eV. Finally, there could be yet another explanation for the large amplitude a_1 of the fundamental in the incident APT needed to reconcile the experiment and theory. In the traditional high harmonic generation setups, the spectral filters and the reflectiveness of XUV mirrors are expected to attenuate the fundamental frequency by a factor of 10^{-4} to 10^{-5} . One can therefore reasonably expect that sufficient amount of the fundamental may reach the molecular system to affect its time-domain response and NFT spectra.

C. Assignments of the calculated spectra: Near-harmonic and non-harmonic peaks

The comparison between the experimental and the ab initio spectra, discussed in the previous section, offers several insights into the relation between the NFT spectrum and the composition of the incident APTs. We turn now to the assignment of the spectral peaks, which allows one to relate the NFT spectra to the properties of the electronic states excited in the pump probe experiment and to expose the origin of near-harmonic and non-harmonic

spectral peaks. Our discussion is based on the calculations using the amplitude Set 1 and $\omega_0 = 1.55$ eV: The spectrum $I_{C^+}(\omega_{\text{NFT}})$, calculated with these settings, shares many principal features with the experimental spectrum.

Appendix B sets the stage for the discussion and summarizes the derivations of analytic expressions for $I_{\text{ion}}(\omega_{\text{NFT}})$ which can be used to guide the spectral assignment. Specifically, Eqs. (B6) and (B7) provide explicit dependence of the spectral intensity on the NFT frequency ω_{NFT} , on the transition frequencies between electronic states, $\Delta_{fi} = \epsilon_{0f} - \epsilon_{0i} > 0$, and on the harmonic frequencies ω_n of the APT components. They are derived using the approximation akin to the temporarily non-overlapping pump and probe pulses, familiar in the context of ultrafast pump probe spectroscopies.^{52,58,75-77} The accuracy of the approximation of Eq. (B6) is illustrated in Fig. 6. Most of the approximate spectral lines (black) are located at the positions of the numerically exact peaks (red). The intensities, which are more sensitive to the coherent two photon effects, are less accurate but the overall spectrum is reasonably reproduced.

The NFT spectrum derived in Appendix B is a superposition of the ionizations of the parent molecule and subsequent excitations into the final dissociative state. It is therefore natural to label the NFT peaks using electronic pairs (i, f) comprising the ionized state(s) i of CO_2^+ , reached in the reaction $\text{CO}_2 \rightarrow \text{CO}_2^+(i)$, and the final dissociative state(s) f of $\text{CO}_2^+(f)$ contributing to the observed C^+ or O^+ signals. The second set of labels are the harmonic assignments indicating the photon frequencies ω_n promoting specific transitions leading to the ionization and dissociation. In practice, we scan the sums in Eq. (B6) for the terms making the largest contribution at a specified ω_{NFT} .

The assignments of the calculated spectrum in terms of these attributes are summarized in Fig. 6. The intermediate states in the ionization step include the ground electronic state of CO_2^+ , $\tilde{X}^2\Pi_g$ as well as the first excited doublet state $\tilde{A}^2\Pi_u$. The final electronic states contributing to the fragment ion signal belong to the series $n^2\Pi_g$ and $n^2\Pi_u$.

In fact, two distinct assignment schemes emerge for the spectral peaks — and they are best illustrated using Eq. (B7) which is valid for the specific case of only one intermediate ionized state i contributing to the dissociation via the final state f . The spectrum $I_{C^+}(\omega_{\text{NFT}})$

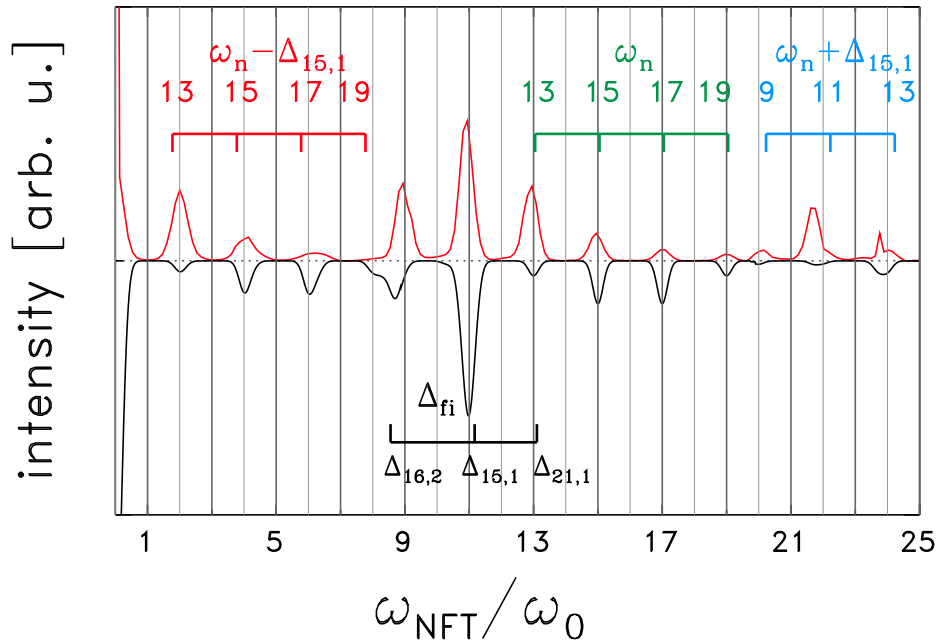


FIG. 6: Comparison of the numerically exact quantum mechanical NFT spectrum (red line) with the approximation of Eq. (B6) (black line). All calculations are performed for $I_{C+}(\omega_{\text{NFT}})$ using APTs with the amplitude Set 1. The fundamental frequency is $\omega_0 = 1.55$ eV. Combs show the assignments in terms of the harmonic frequencies ω_n and the energy differences Δ_{fi} between the ionization and the final dissociation states. States contributing to the assigned peaks are numbered as in Table I: $1 = 1^2\Pi_g$, $2 = 1^2\Pi_u$, $15 = 8^2\Pi_u$, $16 = 10^2\Pi_g$, and $21 = n^2\Pi_u$. Thick (thin) vertical lines indicate odd (even) integer harmonic orders $\omega_{\text{NFT}}/\omega_0$.

in this case consists of two additive contributions. The first is given by

$$\begin{aligned}
 & (\mu_{fi}\mu_{i0})^2 \sum_{n_1, n_2, n_3, n_4} a_{n_1} a_{n_2} a_{n_3} a_{n_4} \mathcal{A}_{n_2, n_4} L_{n_1}(\Delta_{fi}) L_{n_3}(\Delta_{fi}) \\
 & \times \left\{ 4\delta_\tau(\omega_{\text{NFT}}) + 2\delta_\tau(\omega_{\text{NFT}} - \Delta_{fi}) + 2\delta_\tau(\omega_{\text{NFT}} + \Delta_{fi}) \right\}. \quad (28)
 \end{aligned}$$

Here $L_{n_i}(\Omega) = e^{-(\Omega - \omega_{n_i})^2 T^2 / 4P}$ are the Gaussian Fourier images of the time envelope function $L_{n_i}(t, \tau)$ of the APTs defined in Eqs. (5)–(7). The transition is mediated by four photons with harmonic frequencies n_1 , n_2 , n_3 , and n_4 . The resulting NFT spectral peaks are located at $\omega_{\text{NFT}} = 0$ (the zero peak which we do not consider) and at the energy differences between the intermediate ionized and the final dissociative states, $\omega_{\text{NFT}} = \pm\Delta_{fi}$. They are denoted δ_τ because their width is only controlled by the maximum delay time in the time signal, and can potentially be made narrow (delta-function like) by increasing τ_{max} . Note that these

spectral peaks can appear at non-harmonic frequencies if the energy Δ_{fi} is off resonance. The calculation with the Eq. (B6) recognizes two such spectral lines in Fig. 6: One near $\omega_{\text{NFT}} \approx 9\omega_0$ and the other at $11\omega_0$. They belong to the strong central triad discussed in the previous section. We also use this assignment for the third member of the triad, $\omega_{\text{NFT}} \approx 13\omega_0$. The peaks of the triad exemplify the appearance of near harmonic and non-harmonic peaks in the spectrum. The pair of electronic states ($i = \tilde{X}^2\Pi_g$, $f = 8^2\Pi_u$) has, according to Table I, $\Delta_{fi} = 17.08$ eV which is nearly resonant with the harmonic frequency for $n = 11$ (17.05 eV). It gives rise to an intense line at this harmonic order. The pair of states ($i = \tilde{A}^2\Pi_u$, $f = 10^2\Pi_g$) is spaced by 13.49 eV, which is off resonance with respect to the harmonic frequency $\omega_9 = 13.95$ eV. The detuning affects the intensity of this off-resonance non-harmonic line. Indeed, the Gaussian prefactors $L_{n_1}(\Delta_{fi})L_{n_3}(\Delta_{fi})$ suppress large deviations of Δ_{fi} from integers $n_1 = n_3 = 9$. However, the Gaussians are almost 1.0 eV broad and — additionally — τ_{max} is large (20 fs) in this calculation, so that the intensity of this non-harmonic line becomes appreciable. Finally, the peak near $\omega_{\text{NFT}} \approx 13\omega_0$ can be plausibly assigned to the pair of states ($i = \tilde{X}^2\Pi_g$, $f = n^2\Pi_u$) which are in resonance with the harmonic frequency for $n = 13$ (20.15 eV); the offset is merely 0.1 eV, and the third member of the triad is perceived as a harmonic peak.

The second contribution to the NFT spectrum in Eq. (B7) has a different form:

$$\begin{aligned}
& (\mu_{fi}\mu_{i0})^2 \sum_{n_1, n_2, n_3, n_4} a_{n_1} a_{n_2} a_{n_3} a_{n_4} L_{n_1}(\Delta_{fi}) L_{n_3}(\Delta_{fi}) \\
& \times \left\{ 2L_{n_2}(\omega_{\text{NFT}}) L_{n_4}(\omega_{\text{NFT}}) + L_{n_2}(\omega_{\text{NFT}} - \Delta_{fi}) L_{n_4}(\omega_{\text{NFT}} - \Delta_{fi}) \right. \\
& \left. + L_{n_2}(\omega_{\text{NFT}} + \Delta_{fi}) L_{n_4}(\omega_{\text{NFT}} + \Delta_{fi}) \right\} \tag{29}
\end{aligned}$$

There are three sets of peaks associated with this contribution: One set is located at the original harmonic frequencies, $\omega_{\text{NFT}} \approx \omega_{n_2}$ or ω_{n_4} . In Fig. 6, they are shown with the green comb. These peaks are locked on the spectral composition of the incident APTs and have little to no dependence on the ionic energy levels. The third member of the strong triad at $13\omega_0$ contains a low intensity contribution of this type. In the second set, these harmonic peaks are shifted to lower energies by the energy difference Δ_{fi} . In Fig. 6, they are shown with the red comb, and the electronic states are again $i = \tilde{X}^2\Pi_g$ and $f = 8^2\Pi_u$. Because the energy spacing Δ_{fi} is in resonance with ω_{11} , the shifted peaks appear at even harmonics between $n = 2\omega_0$ and $n = 8\omega_0$ and are interpreted as difference peaks in the NFT spectra.

According to Eq. (29), their intensity is one half the intensity of the unshifted harmonic peaks. In the third set, the harmonic peaks are shifted to higher energies by the same amount Δ_{fi} . They are located at high NFT frequencies and marked with the blue comb. In the simple approximation which we are using, their information content is the same as in spectral peaks shifted to low ω_{NFT} . In the present calculation, the peaks of all three sets, even the shifted ones, appear near the integer harmonic orders, either even or odd. This is because the electronic states involved in the optical transitions within the ion are in resonance with one harmonic frequency. However, each NFT peak in Eq. (29) is a product of four Gaussian factors L_{n_i} , and each Gaussian has a width of the order of $\omega_0/2$. Thus, peaks located at non-harmonic frequencies can in principle be expected for the shifted lines. In fact, deviations from integer harmonic orders can be seen for the peaks at $\sim 4\omega_0$ and $\sim 6\omega_0$, as well as $\sim 24\omega_0$. These deviations can be related to the specific electronic transitions in the molecular ion.

Spectral peaks at different NFT frequencies can be further characterized by the ranges of pump probe delay times, at which they are formed. The relation between ω_{NFT} and τ is visualized using the so-called spectrogram

$$S_{C+}(\omega_{\text{NFT}}, t) = \int I_{C+}(\tau)h(\tau - t)e^{i\omega_{\text{NFT}}\tau} d\tau, \quad (30)$$

which is a moving window Fourier transform of the pump probe signal. Here $h(\tau) = \exp(-\tau^2/2\tau_0^2)$ is the Gaussian window function. In the spectrogram $S_{C+}(\omega_{\text{NFT}}, t)$, shown in Fig. 7, the delay time and the NFT frequency domains are represented in the same plot at the expense of the resolution which is smeared along both axes.⁷⁸⁻⁸⁰ The time resolution τ_0 in the plot is 0.9 fs and corresponds to the frequency resolution of $\tau_0^{-1} = 0.80$ eV, about half the fundamental frequency ω_0 .

All major spectral peaks can be clearly recognized in the spectrogram, and they acquire an additional — time delay — dimension. The spectrogram provides a different perspective on the assignment and helps to identify spectral features observed over the same ranges of the delay times. For example, the peaks in the strong central triad $9\omega_0 - 11\omega_0 - 13\omega_0$ have similar spectrograms and collect their intensities over a broad time delay range from -5.0 fs to +5.0 fs. This is an additional reason to assign them using one common assignment scheme as done in Fig. 6. The peaks at $2\omega_0$ and at $22\omega_0$ extend over a similarly broad time delay range — they both belong follow the assignment in terms of $\omega_n \pm \Delta_{fi}$ and share the

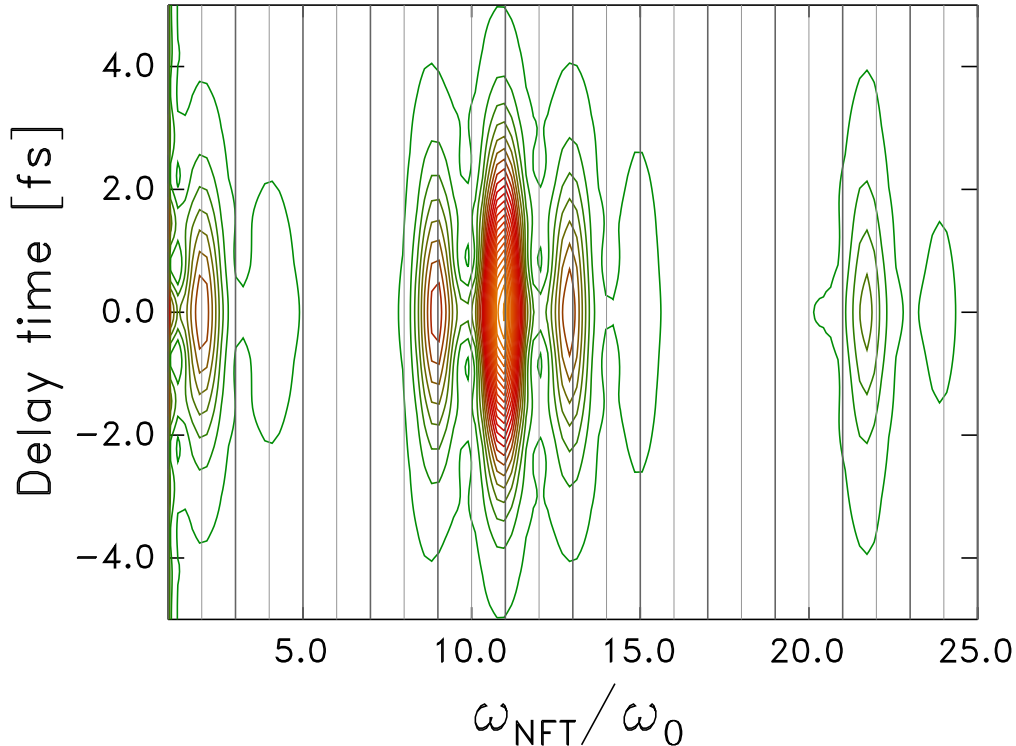


FIG. 7: The spectrogram $S_{C^+}(\omega_{\text{NFT}}, t)$ as defined in Eq. (30), with ω_{NFT} plotted in the units of ω_0 . Red contours correspond to the maxima. The calculations are performed using APTs with the amplitude Set 1. The fundamental frequency in the calculations is $\omega_0 = 1.55$ eV. Vertical lines mark even and odd harmonic orders.

electronic states f and i with the central peak of the triad. For the weaker peaks in the spectrum, the relationships within spectral groups are less straightforward. For example, the peaks at $\sim 4\omega_0$, $15\omega_0$, and $\sim 24\omega_0$ are due to short delay times $|\tau| \leq 2.0$ fs. The spectrogram indicates that they might belong to a separate assignment group which we were not able to identify yet.

In summary, the developed approach provides a reasonable description of NFT spectra of CO_2 , shows their relation to the experiment, and rationalizes the spectral assignments demonstrating the origin of near harmonic and non-harmonic peaks in the spectra.

IV. CONCLUSIONS AND OUTLOOK

In this paper, we outlined a quantum mechanical approach to modeling attosecond NFT spectra of CO_2 ionizing to CO_2^+ . The approach combines perturbation theory for the molecule-light interaction with ab initio calculations of the electronic energy levels of CO_2^+ .

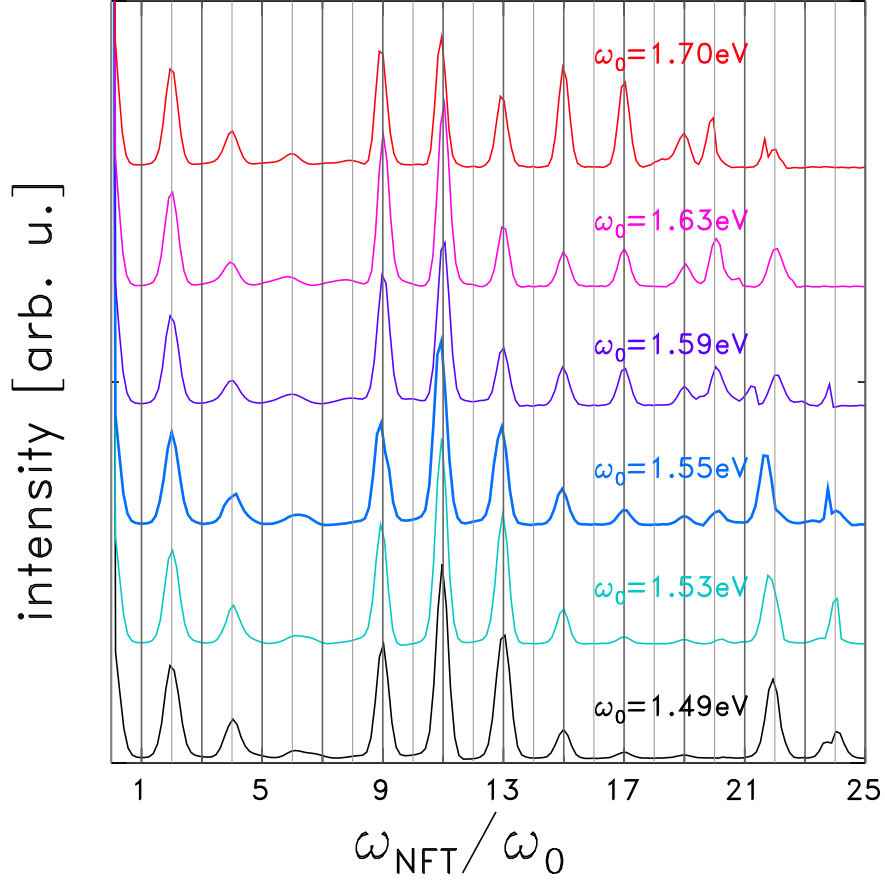


FIG. 8: Ab initio pump probe NFT spectra $I_{C^+}(\omega_{\text{NFT}})$ of CO_2 for a set of fundamental harmonic frequencies ω_0 . The incident APTs are constructed using the amplitude Set 1. All spectra are normalized to the area within the region of $\omega_{\text{NFT}} \leq 25.0$ eV. Thick (thin) vertical lines indicate odd (even) integer values of the ratio $\omega_{\text{NFT}}/\omega_0$.

The ab initio calculations are performed using accurate MRCI method accounting for the electron correlation, but in this work they are limited to the Franck-Condon zone — so that the resulting ladder of electronic levels of CO_2^+ represents a ‘toy model’ of the molecular ion. The main results can be summarized as follows:

1. One-dimensional NFT spectra of CO_2 are calculated for two different incident APTs and compared with the available experimental spectra. Several features of the experiment, including the positions and intensity patterns of the main harmonic spectral peaks, the presence of the difference frequency peaks, and the origin of the low intensity contribution at all harmonic orders, are reproduced and/or explained.
2. The calculations give an overview of the NFT spectrum outside the experimental

frequency window, for $\omega_{\text{NFT}} \geq 25.0 \text{ eV}$, where strong excitations can be expected.

3. A set of approximate analytical expressions for the spectral intensity is derived, demonstrating how the NFT spectral intensity depends on the frequency ω_{NFT} , the harmonic frequencies ω_n of the APT components, and the transition frequencies between electronic states. These expressions guide the assignment of the spectral peaks.
4. The calculated NFT spectra are assigned in terms of the participating electronic states and the harmonic photon frequencies. The assignment demonstrates which details of the electronic structure of the CO_2^+ are captured in the NFT experiments. Using spectrograms, the NFT peaks can be additionally attributed to specific ranges of the pump probe delay times.
5. It is shown that spectral peaks at non-harmonic frequencies can be expected, especially if APTs with spectral bandwidths of about 1 eV are used and photoreactions are limited to single ionizations. Non-harmonic NFT spectral peaks carry additional information on the electronic states mediating ionization of the parent molecule and dissociation of the molecular ion.

The main goal of this work was to set up a framework, within which NFT spectra can be calculated and analyzed, and to test this framework for CO_2 . The tests demonstrate that the framework works with reasonable precision and can be used for semi-quantitative predictions, even though CO_2^+ is described using an ab initio toy model. The simplicity of the ab initio calculations limited to a single Franck-Condon geometry makes this framework highly scalable: It can be applied to polyatomic molecules and ions and one can easily scan through various control parameters of the experiment, such as fundamental laser frequency ω_0 , spectral composition of the incident APTs, or the maximum time delay τ_{max} .

An example is provided in Fig. 8 which shows a series of NFT spectra of CO_2 calculated using ω_0 varying from 1.49 eV (bottom spectrum) to 1.73 eV (top spectrum). The main triad $9\omega_0 - 11\omega_0 - 13\omega_0$ is present in all spectra, the intensity distribution between the peaks changes slightly, and the peak at $13\omega_0$ slowly attenuates as ω_0 grows. The peaks at higher integer harmonic orders, present in the incident APTs, clearly become stronger with increasing ω_0 , as more directly ionizing states become energetically accessible from the ground state of the parent CO_2 . The high frequency end of the NFT spectrum above

$19\omega_0$, which stems from the short time delays $|\tau| \leq 2$ fs and in which the concerted two-photon effects are pronounced, demonstrates a strong dependence on ω_0 , with multiple non-harmonic contributions. In contrast, the low frequency region of the difference frequency peaks is stable, and the peaks $2\omega_0$ and $\sim 4\omega_0$ change neither position nor intensity. Exception is the weaker non-harmonic difference peak which moves between $6\omega_0$ and $7\omega_0$. Figure 8, together with the approximate assignment schemes illustrated in Fig. 6, could in principle be used as a starting point for spectral inversion analysis, in which the electronic states of the dissociating ion are reconstructed from the NFT spectra.

It is highly desirable to extend the developed framework and to replace the toy model based on the electronic state ladder with realistic and interacting potential energy surfaces. This extension, which will be presented in a separate publication, removes two main limitations of the discussed approach. First, it allows calculations of two-dimensional NFT spectra as functions of both fragment kinetic energy and ω_{NFT} . Appendix A provides the necessary formal expressions. Second, vibronic interactions between electronic states become naturally incorporated into the model so that one can analyze the sensitivity of the NFT spectra to non-adiabatic interactions in the parent molecule and in the molecular ion. The time scales and the atomistic mechanisms of ultrafast photoreactions mediated by the vibronic interactions are actively explored^{81,82} across a wide range of applications from advanced energy materials⁸³ to photoprotective mechanisms in biochromophores.^{84,85} In CO_2 and CO_2^+ , non-adiabatic interactions affect not only the absorption and ionization profiles but also the lifetimes of electronically excited species, and the dissociation mechanisms can be controlled by vibronic as well as spin-orbit (i.e. relativistic) interactions.

Appendix A: Two-dimensional NFT signals

After the interaction with two APTs, the excited ion $(\text{CO}_2^+)^{**}$ and the photoelectron are in the state $\Psi_I(t|E_k, \tau)$. We first consider one electronic state $|f\rangle$ of CO_2^+ which dissociates into an arrangement channel with the detected fragment, and restrict the description to 2-body arrangement channels, as indicated in Eq. (3). In this case, one of the dissociation fragments is diatomic and its internal state is characterized by rovibrational quantum numbers, which we collectively denote n_f , and by the internal energy $\epsilon_{\text{int}}(n_f)$. Quantum numbers n_f label individual dissociation channels of $(\text{CO}_2^+)^{**}$ in the state $|f\rangle$ in the con-

sidered arrangement channel. The corresponding dissociation threshold is D_f . Thresholds relevant for the NFT experiments on CO_2 are illustrated in Fig. 2.

Suppose that the final energy of $(\text{CO}_2^+)^{**}$ after the absorption of two photons has a value of ϵ_f lying above D_f . In the dissociation channel, this energy is shared between the (center of mass) recoil kinetic energy ϵ_{kin} and the internal excitation:

$$\epsilon_f = \epsilon_{\text{kin}} + \epsilon_{\text{int}}(n_f) > D_f. \quad (\text{A1})$$

The final rovibrational distribution and the final kinetic energy distribution are complementary and can be recalculated from one another using the energy conservation.

The state of the dissociating fragments is a linear combination of the scattering states⁸⁶ ψ_{f,k_f,n_f}^- , corresponding to the total energy ϵ_f . The probability amplitude for the fragment to be in a state with energy ϵ_f and wave vector k_f (and the kinetic energy $\epsilon_{\text{kin}}(k_f) = k_f^2/2\mu$), while the diatomic fragment is in the internal state n_f , is given by the matrix element

$$\gamma(\epsilon, k_f, n_f | E_k, \tau) = \langle \psi_{f,k_f,n_f}^- | \langle \phi_f^+ \psi_k^e | \Psi_I(t \rightarrow \infty | E_k, \tau) \rangle. \quad (\text{A2})$$

This expression is akin to the photodissociation matrix element⁸⁷ which contains the dynamical information on the dissociation process.^{88,89} The above expression is applied to the ionizing system, and the projection on $\langle \phi_f^+ \psi_k^e |$ additionally specifies that the ejected photoelectron leaves with the energy E_k .

The partial cross section to produce the detected fragment ion in a given dissociation channel n_f describes the rovibrational state distribution — and equivalently the kinetic energy distribution — for the fixed energy ϵ_f . It is given by the square of the matrix element $\int dE_k |\gamma(\epsilon, k_f, n_f | E_k, \tau)|^2$ integrated over all possible photoelectron energies. However, this kinetic energy distribution is not accessible in the multiphoton NFT spectroscopic experiment. The 2D NFT signal as measured, for example, in Ref. 46, is additionally summed over all possible final energies ϵ_f and all final electronic states $|f\rangle$ contributing to the detected dissociation fragment:

$$I_{\text{ion}}^{2D}(\epsilon_{\text{kin}}, \tau) = \sum_f \int_{D_f}^{\infty} d\epsilon_f \int_0^{\infty} dE_k |\gamma(\epsilon, k_f, n_f | E_k, \tau)|^2. \quad (\text{A3})$$

Evaluation of the photodissociation matrix element $\gamma(\epsilon, k_f, n_f | E_k, \tau)$ requires numerical solution of the Schrödinger equation with the (generally three-dimensional) potential energy surfaces of the dissociative electronic states of CO_2^+ . While the nuclear dynamics for the

photofragment distributions can be efficiently calculated using iterative methods,^{90–92} construction of the multidimensional potential energy surfaces of many densely spaced (and possibly interacting) electronic states in the energy range illustrated in Fig. 2 is a true challenge.^{21,93}

Sum over all channel quantum numbers n_f effectively brings about summation over all fragment kinetic energies and gives the 1D NFT signal, i.e. the total ion yield:

$$I_{\text{ion}}^{1D}(\tau) = \sum_f \sum_{n_f} \int_{D_f}^{\infty} d\epsilon \int_0^{\infty} dE_k |\gamma(\epsilon, k_f, n_f | E_k, \tau)|^2. \quad (\text{A4})$$

The scattering basis states are complete, and this expression can be rewritten in terms of the populations of the final electronic states integrated over the photoelectron kinetic energy:

$$I_{\text{ion}}^{1D}(\tau) = \sum_f \int_0^{\infty} dE_k \langle \Psi_I^c(t \rightarrow \infty | E_k, \tau) | \phi_f^+ \psi_k^e \rangle \langle \phi_f^+ \psi_k^e | \Psi_I^c(t \rightarrow \infty | E_k, \tau) \rangle. \quad (\text{A5})$$

This expression is practically identical to the total ion yield defined in Eqs. (16) and (17) of the main text. The appearance threshold A_{ion} for the detected ion fragment corresponds to the lowest energy ϵ_f (and the lowest state $|f\rangle$) for which the amplitude $\gamma(\epsilon, k_f, n_f | E_k, \tau)$ does not vanish. The subscript c on the wave function in Eq. (A5) is a remainder that only projections on the continuum states ψ_{f,k_f,n_f}^- are considered in each state $|f\rangle$.

Appendix B: Analytic expressions for 1D NFT signals

The quantum mechanical expressions for the NFT signals $I_{\text{ion}}(\tau)$ and $I_{\text{ion}}(\omega_{\text{NFT}})$, as described in Sect. IID [see Eqs. (17), (18), and (21)—(24)], are well suited for numerical calculations. One can cast them into a different form more appropriate for the analysis and assignment of the spectral peaks. This appendix summarizes analytic expressions for $I_{\text{ion}}(\omega_{\text{NFT}})$ which help to rationalize the NFT spectra. The implications for the spectral assignments are discussed in Sect. IIIC.

For simplicity, we consider only the photoreaction pathway in which the parent molecule is ionized already with the first photon. The second order pump probe amplitude $c_j(v_j; E_k, \tau)$ is given by the Eq. (21). Changing the variables to $y = t_1 - t_0$ in the inner integral with y running from 0 to ∞ , using the Fourier transform of the APT electric field, $\mathcal{E}(\Omega; \tau)$, and

invoking the convolution theorem, the amplitude $c_j(v_j; E_k, \tau)$ can be re-written as

$$c_j(v_j; E_k, \tau) = \frac{1}{i^2} \sum_{i \neq j} \sum_{v_i} \mu_{ji} \mu_{i0}(E_k) \times \int_{-\infty}^{\infty} \frac{d\Omega}{2\pi} \mathcal{E}(\epsilon_{vj} - \Omega; \tau) \frac{i \langle v_j | v_i \rangle \langle v_i | 0 \rangle}{\Omega - \epsilon_{vi} + i0} \mathcal{E}(\Omega + E_k - \epsilon_0; \tau). \quad (\text{B1})$$

This (still exact) pump probe amplitude is given by the convolution of two Fourier images of the laser electric field and the pole factor $i(\Omega - \epsilon_{vi} + i0)^{-1}$ corresponding to the Fourier transform of $e^{-i\epsilon_{vi}y}$ times the Heaviside step function $\Theta(y)$.⁵⁸ The Fourier transform of the laser field is given by

$$\mathcal{E}(\Omega; \tau) = \sum_n' a_n L_n(\Omega) (1 + e^{i\Omega\tau}), \quad (\text{B2})$$

with $L_n(\Omega)$ being the Fourier image of the time envelope function $L_n(t, \tau)$ defined through the Eqs. (5), (6), and (7).

The integral over Ω has a suggestive form for the use of contour integration in the complex plane and the residue theorem. The success of this approach depends on the actual shape of the function $L_n(\Omega)$. In the main text, computations are performed using the Gaussian time envelope $L_n(t, \tau)$. The function $L_n(\Omega)$ is then also a Gaussian,

$$L_n(\Omega) = e^{-(\Omega - \omega_n)^2 T^2 / 4P}, \quad (\text{B3})$$

and the integral in Eq. (B1) leads to the Hilbert transform of a Gaussian function, which does not have a simple analytic representation.⁹⁴ Other envelope functions can be easier to handle. Example is the exponential decay envelope^{75,95}

$$L_n(t, \tau) = e^{-P|t-\tau|/T}.$$

Its Fourier image

$$L_n(\Omega) = \frac{P/T}{(\Omega - \omega_n)^2 + (P/T)^2}$$

has a Lorentzian lineshape and therefore a simple residue structure which makes the integration of Eq. (B1) in the complex plane straightforward. The subsequent integrations in

$$\int_0^{\infty} dE_k \int d\tau e^{i\omega_{NFT}\tau} |c_j|^2. \quad (\text{B4})$$

are also analytical. The resulting expressions, however, are awkward and tedious to analyze.

In fact, the nature of spectral peaks in the quantum mechanical NFT spectra can be exposed using an approximation. We replace the pole factor in Eq. (B1) with $-i\pi\delta(\Omega -$

ϵ_{vi}) and ignore the principal value contribution. This is similar to the approximation of temporarily non-overlapping pump and probe pulses, familiar in the context of ultrafast pump-probe spectroscopies.^{52,58,75,76} With this approximation, the pump probe amplitude $c_j(v_j; E_k, \tau)$ can be easily evaluated, and its square is written as

$$\begin{aligned}
|c_j(v_j; E_k, \tau)|^2 &= \sum_{i_1, i_2 \neq j} \sum_{v_{i_1}, v_{i_2}} \sum_{n_1, n_2, n_3, n_4} \mu_{ji_1} \mu_{i_1 0}(E_k) \mu_{ji_2} \mu_{i_2 0}(E_k) \\
&\times \langle v_j | v_{i_1} \rangle \langle v_{i_2} | v_j \rangle \langle v_{i_1} | 0 \rangle \langle 0 | v_{i_1} \rangle a_{n_1} a_{n_2} a_{n_3} a_{n_4} \\
&\times L_{n_1}(\epsilon_{vj} - \epsilon_{vi_1}) L_{n_2}(\epsilon_{vi_1} - \epsilon_0 + E_k) L_{n_3}(\epsilon_{vj} - \epsilon_{vi_2}) L_{n_4}(\epsilon_{vi_2} - \epsilon_0 + E_k) \\
&\times \left[(1 + e^{i(\epsilon_{vj} - \epsilon_{vi_1})\tau}) (1 + e^{i(\epsilon_{vi_1} - \epsilon_0 + E_k)\tau}) \right. \\
&\quad \left. (1 + e^{-i(\epsilon_{vj} - \epsilon_{vi_2})\tau}) (1 + e^{-i(\epsilon_{vi_2} - \epsilon_0 + E_k)\tau}) \right]. \tag{B5}
\end{aligned}$$

In this expression, we expand the electric fields as sums over the odd harmonics, as in Eq. (B2), and assume that the coefficients $\{a_n\}$ and the TDMs are real. The dependence of the probability $|c_j|^2$ on the delay time τ and the photoelectron kinetic energy E_k is now explicit, and the integrals in Eq. (B4) can be performed directly. Let us define the energy differences between the molecular or ionic states as $\Delta_{ji} = \epsilon_{vj} - \epsilon_{vi}$ and $\Delta_{i0} = \epsilon_{vi} - \epsilon_0$. Then the NFT spectrum, obtained after the integrations, reads as

$$\begin{aligned}
I_{\text{ion}}(\omega_{\text{NFT}}) &= \sum_j \sum_{\epsilon_{vj} > A_{\text{ion}}} \sum_{i_1, i_2 \neq j} \sum_{v_{i_1}, v_{i_2}} \sum_{n_1, n_2, n_3, n_4} \mu_{ji_1} \mu_{i_1 0} \mu_{ji_2} \mu_{i_2 0} \\
&\times \langle v_j | v_{i_1} \rangle \langle v_{i_2} | v_j \rangle \langle v_{i_1} | 0 \rangle \langle 0 | v_{i_1} \rangle a_{n_1} a_{n_2} a_{n_3} a_{n_4} \\
&\times \left[L_{n_1}(\Delta_{ji_1}) L_{n_3}(\Delta_{ji_2}) \frac{1}{2} \sqrt{\frac{2\pi P}{T^2}} e^{-T^2(s_{n_2} - s_{n_4})^2/8P} \left(1 + \text{erf} \left(\frac{T}{\sqrt{2P}} \overline{s_{n_2, n_4}} \right) \right) \right. \\
&\times \left\{ 2\delta_\tau(\omega_{\text{NFT}}) + \delta_\tau(\omega_{\text{NFT}} \pm \Delta_{ji_1}) + \delta_\tau(\omega_{\text{NFT}} \pm \Delta_{ji_2}) + \delta_\tau(\omega_{\text{NFT}} \pm \Delta_{i_1 i_2}) \right\}_1 \\
&+ L_{n_1}(\Delta_{ji_1}) L_{n_3}(\Delta_{ji_2}) \\
&\times \left\{ L_{n_2}(\omega_{\text{NFT}}) L_{n_4}(\omega_{\text{NFT}} - \Delta_{i_1 i_2}) + L_{n_2}(\omega_{\text{NFT}} + \Delta_{i_1 i_2}) L_{n_4}(\omega_{\text{NFT}}) \right. \\
&\quad \left. + L_{n_2}(\omega_{\text{NFT}} - \Delta_{ji_1}) L_{n_4}(\omega_{\text{NFT}} - \Delta_{ji_2}) + L_{n_2}(\omega_{\text{NFT}} + \Delta_{ji_1}) L_{n_4}(\omega_{\text{NFT}} + \Delta_{ji_2}) \right\}_2 \left. \right]; \tag{B6}
\end{aligned}$$

$$s_{n_2} = \omega_{n_2} - \Delta_{i_1 0};$$

$$s_{n_4} = \omega_{n_4} - \Delta_{i_2 0};$$

$$\overline{s_{n_2, n_4}} = \frac{1}{2}(s_{n_2} + s_{n_4}).$$

Here $\text{erf}(x)$ is the standard error integral.⁹⁶ The expression holds for any lineshape function $L_n(\Omega)$, and we shall use Gaussians as in Eq. (B3). The NFT spectrum arises as a superposition of ionizations of the parent molecule into the intermediate ionic states i_1 and i_2 which are then further excited into a dissociative state j . There are two groups of NFT spectral peaks in this expression, corresponding to the two types of τ -dependent terms in Eq. (B5). The first group — placed inside the curly brackets $\{\dots\}_1$ — includes spectral peaks which are located at the energy differences between the intermediate ionized and the final dissociative states, $\omega_{\text{NFT}} = \pm\Delta_{ji}$. Their width is controlled by the maximum delay time in Eq. (18), and can potentially be made narrow (delta-function like) by increasing τ_{max} . These NFT peaks are denoted as δ_τ . They stem from the terms in $|c_j(v_j; E_k, \tau)|^2$ with the exponential phase factors independent of E_k , such as $e^{-i\Delta_{ji}\tau}$ for example. The positions of these peaks need not coincide with the multiples of the fundamental harmonic frequency ω_0 . The second group includes terms — placed inside the curly brackets $\{\dots\}_2$ — which are products of two Gaussian functions L_n . Each Gaussian factor peaks at $\omega_{\text{NFT}} = \omega_n \pm \Delta_{ji}$; the spectral width is determined by the reciprocal of the APT temporal width T [see Eq. (B3)]. These spectral lines stem from the τ -dependent terms with the exponential phase factors explicitly depending on E_k . The positions of these peaks tend to cluster around the harmonic frequencies $n\omega_0$. Note that the widths of different lines in the actual NFT spectrum are expected to be sensitive to either τ_{max} or T .

The accuracy of the approximation of Eq. (B6) is illustrated in Fig. 6 in the main text: Most of the approximate spectral lines (black) accurately reproduce the positions of the numerically exact peaks (red). The agreement is worse for the intensities, which are more sensitive to the coherent two photon effects, but the overall spectrum is quite well recognizable. This makes the approximation useful in the analysis of the origin of near harmonic as well as non-harmonic spectral peaks. The peaks assigned Δ_{fi} stem from the terms in $\{\dots\}_1$; the peaks assigned ω_n and $\omega_n \pm \Delta_{fi}$ are due to the terms in $\{\dots\}_2$. In particular, peaks around $\omega_{\text{NFT}}/\omega_0 = 9, 22, 24$ deviating from the integer harmonic orders are reproduced.

Although the NFT spectrum in the above equation is already an approximation, it is still rather bulky and awkward to use in spectral assignments. In order to simplify the discussion of the assignment in Sect. III C, we introduce yet another approximation and assume that the ionizations in Eq. (B6) terminate in the same ionic state $i_1 = i_2 = i$. This is a realistic scenario, at least for the amplitude Set 1 and $\omega_0 = 1.55$ eV. We also consider only the ground

vibrational states in all electronic states, drop sums over vi , and rename the final dissociative states $\epsilon_j > A_{\text{ion}}$ as f . The NFT spectrum is then given by

$$\begin{aligned}
I_{\text{ion}}(\omega_{\text{NFT}}) &= \sum_f \sum_{i \neq f} \sum_{n_1, n_2, n_3, n_4} (\mu_{fi} \mu_{i0})^2 a_{n_1} a_{n_2} a_{n_3} a_{n_4} \\
&\times L_{n_1}(\Delta_{fi}) L_{n_3}(\Delta_{fi}) \left[\frac{1}{2} \sqrt{\frac{2\pi P}{T^2}} e^{-T^2(s_{n_2} - s_{n_4})^2/8P} \left(1 + \operatorname{erf} \left(\frac{T}{\sqrt{2P}} s_{n_2, n_4} \right) \right) \right] \\
&\times \left\{ 4\delta_\tau(\omega_{\text{NFT}}) + 2\delta_\tau(\omega_{\text{NFT}} - \Delta_{fi}) + 2\delta_\tau(\omega_{\text{NFT}} + \Delta_{fi}) \right\}_1 \\
&+ \left\{ 2L_{n_2}(\omega_{\text{NFT}}) L_{n_4}(\omega_{\text{NFT}}) + L_{n_2}(\omega_{\text{NFT}} - \Delta_{fi}) L_{n_4}(\omega_{\text{NFT}} - \Delta_{fi}) \right. \\
&\quad \left. L_{n_2}(\omega_{\text{NFT}} + \Delta_{fi}) L_{n_4}(\omega_{\text{NFT}} + \Delta_{fi}) \right\}_2. \tag{B7}
\end{aligned}$$

The simplified spectrum again consists of two groups of spectral peaks, those located at the electronic energy differences $\pm\Delta_{fi}$, and those located at the unshifted (ω_n) and shifted, ($\omega_n \pm \Delta_{fi}$), harmonic frequencies. There can therefore be a substantial number of spectral peaks located at non-harmonic frequencies if Δ_{fi} is not exactly equal to a multiple of ω_0 . Moreover, the Gaussian factors indicate that off-resonance excitations within the spectral width of L_n can be encountered in an NFT spectrum. This width is of the order of 1 eV (i.e. of the order of ω_0) for the typical experimental APTs, so that deviations from the harmonic frequencies within $\pm\omega_0$ are not unexpected.

Note that the factors L_n , allowing non-resonant excitations within their spectral widths, carry as arguments only the energy differences Δ_{fi} between the ionic states involved in the optical excitation of the ion; the energy differences between the initial state of the parent molecule and the ionized state, $\Delta_{i0} = \epsilon_i - \epsilon_0$, are not involved in the final expressions. This is an intrinsic feature of the photochemical pathway of Eq. (1): The mismatch between Δ_{i0} and the harmonic frequency $\omega_n > \Delta_{i0}$ can be compensated by the kinetic energy $E_k = \omega_n - \Delta_{i0}$ of the photoelectron ejected in the first (ionization) step.

The approximate expressions for the NFT spectra, Eqs. (B6) and (B7), are further discussed in Sect. IIIC and used to explain the assignment scheme for NFT spectra.

Acknowledgments

This work was partly supported by the U.S. Department of Energy, Office of Science, Office of Basic Energy Sciences under Contract No. DE-AC02-76SF00515. S.C. thanks

Tomoya Okino and Yasuo Nabekawa for private communications and for providing experimental 2D NFT spectra of CO₂ in digital format.

- ¹ M. .A. Gharaibeh and D. J. Clouthier, *J. Chem. Phys.* **132**, 114307 (2010).
- ² W. T. Huntress, M. J. McEvan, Z. Karpas and V. G. Anicich, *Astrophys. J. Supp. Ser.* **44**, 481 (1980).
- ³ Up-to-date atmospheric CO₂ concentrations can be found at [<http://www.esrl.noaa.gov/gmd/ccgg/trends>].
- ⁴ J. B. Jeffries, C. Schulz, D. W. Mattison, M. A. Oehlschlaeger, W. G. Bessler, T. Lee, D. F. Davidson and R. K. Hanson, *Proc. Combust. Inst.* **30**, 1591 (2005).
- ⁵ P. D. Feldman, E. B. Burgh, S. T. Durrance and A. F. Davidsen, *Astrophys. J.* **538**, 395 (2000).
- ⁶ V. Vuitton, R. V. Yelle and J. Cui, *J. Geophys. Res. (Planets)* **113**, 5007 (2008).
- ⁷ G. Herzberg. *Molecular Spectra and Molecular Structure III. Electronic Spectra and Electronic Structure of Polyatomic Molecules*. Van Nostrand, Princeton, (1967).
- ⁸ G. Lawrence, *J. Chem. Phys.* **56**, 3435 (1972).
- ⁹ I. Reineck, C. Nohre, R. Maripuu, P. Lodin, S. H. Al-Shamma, H. Veenhuizen, L. Karlsson and K. Siegbahn, *Chem. Phys.* **78**, 311 (1983).
- ¹⁰ C. Cossart-Magos, M. Jungen and F. Launay, *Mol. Phys.* **61**, 1077 (1987).
- ¹¹ Y.-F. Zhu and R. J. Gordon, *J. Chem. Phys.* **92**, 2897 (1990).
- ¹² M. Brommer, G. Chambaud, E.-A. Reinsch, P. Rosmus, A. Spielfiedel, N. Feautrier and H.-J. Werner, *J. Chem. Phys.* **94**, 8070 (1991).
- ¹³ A. Spielfiedel, N. Feautrier, C. Cossart-Magos, G. Chambaud, P. Rosmus, H.-J. Werner and P. Botschwina, *J. Chem. Phys.* **97**, 8382 (1992).
- ¹⁴ A. Stolow and Y. T. Lee, *J. Chem. Phys.* **98**, 2066 (1993).
- ¹⁵ P. Baltzer, F. T. Chau, J. H. D. Eland, L. Karlsson, M. Lundqvist, J. Rostas, K. Y Tam, H. Veenhuizen and B. Wannberg, *J. Chem. Phys.* **104**, 8922 (1996).
- ¹⁶ J. Liu, W. Chen, C.-W. Hsu, M. Hochlaf, M. Evans, S. Stimson and C. Y. Ng, *J. Chem. Phys.* **112**, 10767 (2000).
- ¹⁷ T. Lyman, *Astrophys. J.* **27**, 87 (1908).
- ¹⁸ Z. Chen, F. Lio, B. Jiang, X. Yang and D. H. Parker, *J. Phys. Chem. Lett.* **1**, 1861 (2010).

- ¹⁹ S. Yu. Grebenshchikov, *J. Chem. Phys.* **137**, 021101 (2012).
- ²⁰ S. Yu. Grebenshchikov and R. Borrelli, *J. Phys. Chem. Lett.* **3**, 3223 (2012).
- ²¹ S. Yu. Grebenshchikov, *J. Chem. Phys.* **138**, 224106 (2013).
- ²² S. Yu. Grebenshchikov, *J. Chem. Phys.* **138**, 224107 (2013).
- ²³ L. Archer, G. Stark, P. Smith, J. Lyons, N. de Oliveira, L. Nahon, D. Joyeux and D. Blackie, *J. Quant. Spectrosc. Radiat. Transfer* **117**, 88 (2013).
- ²⁴ Z. Lu, Y. C. Chang, Q.-Z. Yin, C. Y. Ng and W. M. Jackson, *Science* **346**, 61 (2014).
- ²⁵ Z. Lu, Y. C. Chang, H. Gao, Y. Benitez, Y. Song, C. Y. Ng and W. M. Jackson, *J. Chem. Phys.* **140**, 231101 (2014).
- ²⁶ Y. Song, H. Gao, Y. C. Chang, Z. Lu, C. Y. Ng and W. M. Jackson, *Phys. Chem. Chem. Phys.* **16**, 563 (2014).
- ²⁷ F. Kelkensberg, A. Rouzee, W. Siu, G. Gademann, P. Johnsson, M. Lucchini, R. R. Lucchese and M. J. J. Vrakking, *Phys. Rev. A* **84**, 051404(R) (2011).
- ²⁸ S. Adachi, M. Sato, T. Suzuki and S. Yu. Grebenshchikov, *Phys. Rev. A* **95**, 033422 (2017).
- ²⁹ A. Kamalov, A. L. Wang, P. H. Bucksbaum, D. J. Haxton and J. P. Cryan, *Phys. Rev. A* **102**, 023118 (2020).
- ³⁰ S. Yu. Grebenshchikov, *J. CO2 Utilization* **15**, 32 (2016).
- ³¹ A. J. Traynor and R. J. Jensen, *Ind. Eng. Chem. Res.* **41**, 1935 (2002).
- ³² C. Liu, J. M. Notestein, E. Weitz and K. Gray, *ChemSusChem* **11**, 1163 (2018).
- ³³ S. Yu. Grebenshchikov, *J. Phys. Chem. A* **121**, 4296 (2017).
- ³⁴ J. M. Bowman, *Mol. Phys.* **112**, 2516 (2014).
- ³⁵ S. Yu, D. Yuan, W. Chen, J. Zhou, X. Yang and X. Wang, *J. Chem. Phys.* **151**, 214306 (2019).
- ³⁶ N. Berrah, A. Sanchez-Gonzalez and Z. Jurek et al., *Nat. Phys.* **15**, 1279 (2019).
- ³⁷ K. Ramasesha, S. R. Leone and D. M. Neumark, *Annu. Rev. Phys. Chem.* **67**, 41 (2016).
- ³⁸ E. J. Sie, T. Rohwer, C. Lee and N. Gedik, *Nat. Commun.* **10**, 3535 (2019).
- ³⁹ C. Chen, Z. Tao and A. Carr et al., *Proc. Natl. Acad. Sci. USA* **114**, E5300 (2017).
- ⁴⁰ R. Pazourek, J. Feist, S. Nagele and J. Burgdörfer, *Phys. Rev. Lett.* **108**, 163001 (2012).
- ⁴¹ A. L. Cavalieri, N. Müller, Uphues Th. and V. S. Yakovlev et al., *Nature* **449**, 1029 (2007).
- ⁴² S. Li, T. Driver and A. Al Haddad et al., *J. Phys. B.* **XX**, YYYY (2020).
- ⁴³ S. Tanaka and S. Mukamel, *Phys. Rev. Lett.* **89**, 043001 (2002).
- ⁴⁴ T. Sekikawa, A. Kosuge, T. Kanai and S. Watanabe, *Nature* **432**, 605 (2004).

- ⁴⁵ T. Okino, K. Yamanouchi, T. Shimizu, R. Ma, Y. Nabekawa and K. Midorikawa, *J. Chem. Phys.* **129**, 161103 (2008).
- ⁴⁶ T. Okino, A. Furukawa, T. Shimizu, Y. Nabekawa, K. Yamanouchi and K. Midorikawa, *J. Phys. B: At. Mol. Opt. Phys.* **47**, 124007 (2014).
- ⁴⁷ M. Lewenstein, P. Balcou, M. Yu. Ivanov, Anne L’Huillier and P. B. Corkum, *Phys. Rev. A* **49**, 2117 (1994).
- ⁴⁸ Y. Nabekawa, T. Shimizu, , T. Okino, A. Furukawa, H. Hasegawa, K. Yamanouchi and K. Midorikawa, *Phys. Rev. Lett.* **97**, 153904 (2006).
- ⁴⁹ Y. Nabekawa, T. Shimizu, A. Furukawa and E. J. Takahashi, *Phys. Rev. Lett.* **102**, 213904 (2009).
- ⁵⁰ A. T. J. B. Eppink and D. H. Parker, *Rev. Sci. Instrum.* **68**, 3477 (1997).
- ⁵¹ M. Seel and W. Domcke, *J. Chem. Phys.* **95**, 7806 (1991).
- ⁵² M. Seel and W. Domcke, *Chem. Phys.* **151**, 59 (1991).
- ⁵³ A. P. Hitchcock, C. E. Brion and M. J. van der Wiel, *Chem. Phys.* **45**, 461 (1980).
- ⁵⁴ T. Masuoka, *Phys. Rev. A* **50**, 3886 (1994).
- ⁵⁵ J. A.R. Samson, P.C. Kemeny and G.N. Haddad, *Chem. Phys. Lett.* **51**, 75 (1977).
- ⁵⁶ M. Alagia, P. Candori, S. Falcinelli, M. Lavollee, F. Pirani, R. Richter, S. Stranges and F. Vecchiocattivi, *Phys. Chem. Chem. Phys.* **12**, 5389 (2010).
- ⁵⁷ S. Erattupuzha, S. Larimian, A. Baltuska, X. Xie and M. Kitzler, *J. Chem. Phys.* **144**, 024306 (2016).
- ⁵⁸ G. Stock, R. Schneider and W. Domcke, *J. Chem. Phys.* **90**, 7184 (1989).
- ⁵⁹ In the current context, in which the electronic states of CO_2 and CO_2^+ are treated in the Franck-Condon approximation, only one electronic ionization continuum for all states is considered. This restriction is non-limiting and can be easily removed, as is done, for example, in Refs. 51 and 52. .
- ⁶⁰ Possible polarization of the incident light is not explicitly included in the definitions of the interaction terms. .
- ⁶¹ W. Domcke, *Chem. Phys.* **40**, 171 (1979).
- ⁶² W. Domcke, D. R. Yarkony and H. Köppel, Eds. *Conical Intersections*. World Scientific, Singapore, (2004).
- ⁶³ M. Ogawa, *J. Chem. Phys.* **54**, 2550 (1971).

- ⁶⁴ C. Cossart-Magos, F. Launay and J. E. Parkin, *Mol. Phys.* **75**, 835 (1992).
- ⁶⁵ C. Cossart-Magos, F. Launay and J. E. Parkin, *Mol. Phys.* **103**, 629 (2005).
- ⁶⁶ J. W. Rabalais, J. M. McDonald, V. Scherr and S. P. McGlynn, *Chem. Rev.* **71**, 73 (1971).
- ⁶⁷ H.-J. Werner, P. J. Knowles, G. Knizia, F. R. Manby and M. Schütz, *WIREs Comput. Mol. Sci.* **2**, 242 (2012).
- ⁶⁸ H.-J. Werner, P. J. Knowles, G. Knizia, F. R. Manby, M. Schütz and et al. Molpro, version 2009, a package of ab initio programs, (2009). see <http://www.molpro.net>.
- ⁶⁹ A. Motzke, Z. Lan, C. Woywod and W. Domcke, *Chem. Phys.* **329**, 50 (2006).
- ⁷⁰ W. Eisfeld, *Phys. Chem. Chem. Phys.* **7**, 832 (2005).
- ⁷¹ L.-S. Wang, J. E. Reutt, Y. T. Lee and D. A. Shirley, *J. Electr. Spectr. Rel. Phenomena* **47**, 167 (1988).
- ⁷² C. Winterfeldt, C. Spielmann and G. Gerber, *Rev. Mod. Phys.* **80**, 117 (2008).
- ⁷³ T. Popmintchev, M.-C. Chen, A. Bahabad, M. Gerrity, P. Sidorenko, O. Cohen, I. P. Christov, M. M. Murnane and H. C. Kapteyn, *Proc. Nat. Acad. Sci.* **106**, 10516 (2009).
- ⁷⁴ The attainable upper limit of reliably detected NFT spectra frequencies ω_{NFT} is controlled by the inverse of the time interval over which ionic signal created by the pump and probe APTs is reliably observable. In CO_2 having APTs with time envelopes of 5–7 fs wide, the experimental detection limit is about $\omega_{\text{NFT}} \approx 20 \text{ eV}$.
- ⁷⁵ S. Y. Lee. In *Femtosecond Chemistry*, edited by J. Manz and L. Woste, page 273. (VCH, Berlin, 1995).
- ⁷⁶ T. C. Wehnacht and B. J. Pearson. *Time-resolved spectroscopy. An experimental perspective*. Taylor & Francis Group, Boca Raton, (2019).
- ⁷⁷ Note that explicit expressions for the NFT spectra can be obtained also without approximations using model APTs with an exponential decay envelope $L_n(t, \tau)$ [cf. Eq. (6)]. However, the resulting expression for $I_{\text{ion}}(\omega_{\text{NFT}})$ are long and not very useful for the analysis.
- ⁷⁸ B. R. Johnson and J. L. Kinsey, *J. Chem. Phys.* **91**, 7638 (1989).
- ⁷⁹ K. Hirai, E.J. Heller and P. Gaspard, *J. Chem. Phys.* **103**, 5970 (1995).
- ⁸⁰ M.J.J. Vrakking, D.M. Villeneuve and A. Stolow, *Phys. Rev. A* **54**, R37 (1996).
- ⁸¹ W. Domcke, D. R. Yarkony and H. Köppel, Eds. *Conical Intersections*. World Scientific, Singapore, (2012).
- ⁸² E. G. Champenois, N. H. Shivaram, T. W. Wright, C.-S. Yang, A. Belkacem and J. P. Cryan,

- J. Chem. Phys. **144**, 014303 (2016).
- ⁸³ In *Photophysics of Molecular Materials: From Single Molecules to Single Crystals*, edited by G. Lanzani. (Wiley VCH, Weinheim, 2006).
- ⁸⁴ S. J. Formosinho and L. G. Arnaut, J. Photochem. Photobiol. **75**, 21 (1993).
- ⁸⁵ A. Migani, L. Blancafort, M. A. Robb and A. D. DeBellis, J. Am. Chem. Soc. **130**, 6932 (2008).
- ⁸⁶ A.M. Perelomov and Ya. B. Zel'dovich. *Quantum Mechanics. Selected Topics*. World Scientific, Singapore, (1998).
- ⁸⁷ G. G. Balint-Kurti, Adv. Chem. Phys. **128**, 249 (2004).
- ⁸⁸ D. Picconi and S. Yu. Grebenschchikov, J. Chem. Phys. **148**, 104103 (2018).
- ⁸⁹ D. Picconi and S. Yu. Grebenschchikov, J. Chem. Phys. **148**, 104104 (2018).
- ⁹⁰ D. Picconi and S. Yu. Grebenschchikov, J. Chem. Phys. **141**, 074311 (2014).
- ⁹¹ D. Picconi and S. Yu. Grebenschchikov, Phys. Chem. Chem. Phys. **17**, 28931 (2015).
- ⁹² D. Picconi and S. Yu. Grebenschchikov, Chem. Phys. **481**, 231 (2016).
- ⁹³ S. Yu. Grebenschchikov, Z.-W. Qu, H. Zhu and R. Schinke, Phys. Chem. Chem. Phys. **9**, 2044 (2007).
- ⁹⁴ F. W. King. *Hilbert Transforms*. Cambridge University Press, Cambridge, (2009).
- ⁹⁵ P. Antoine, A. L'Huillier and M. Lewenstein, Phys. Rev. Lett. **77**, 1234 (1996).
- ⁹⁶ M. Abramowitz and I. A. Stegun (Ed.). *Handbook of Mathematical Functions*. Dover, New York, (1970).

TABLE I: The set of ab initio doublet electronic states of CO_2^+ included in the quantum mechanical calculations of NFT spectra. Shown are vertical excitation energies T_e (in eV, relative to the equilibrium of the ground electronic state of CO_2) and the photoionization dipole matrix elements μ_{j0} with the ground electronic state of CO_2 . Calculations are performed using MRD-CI method. Experimental energies (T_e , in eV) and assignments, taken from Ref. 71, are shown where available.

No.	State	T_e (calc)	T_v (exp)	μ_{j0}
1	$1^2\Pi_g$	13.75	13.78	1.66
2	$1^2\Pi_u$	17.57	17.31	1.56
3	$1^2\Sigma_u^+$	18.01	18.08	0.81
4	$1^2\Sigma_g^+$	19.26	19.39	0.79
5	$5^2\Pi_u$	26.64	—	0.52
6	$3^2\Sigma_u^-$	28.23	—	0.00
7	$3^2\Delta_u$	28.27	—	0.04
8	$7^2\Pi_g$	29.50	—	0.10
9	$6^2\Pi_u$	29.51	—	0.08
10	$4^2\Sigma_u^-$	29.98	—	0.00
11	$8^2\Pi_g$	30.12	—	0.06
12	$9^2\Pi_g$	30.57	—	0.07
13	$5^2\Sigma_u^-$	30.59	—	0.00
14	$4^2\Delta_u$	30.62	—	0.01
15	$8^2\Pi_u$	30.83	—	0.18
16	$10^2\Pi_g$	31.06	—	0.12
17	$9^2\Pi_u$	31.55	—	0.11
18	$4^2\Sigma_u^+$	31.78	—	0.13
19	$5^2\Sigma_u^+$	31.79	—	0.04
20	$n^2\Sigma_g^+$	32.10 (32.70)	—	0.07
21	$n^2\Pi_u$	31.56 (34.06)	—	0.06
22	$n^2\Sigma_u^+$	32.50 (35.00)	—	0.02